

# **Coseismic slip distribution of the 1923 Kanto earthquake, Japan**

Fred F. Pollitz<sup>1</sup>, Marleen Nyst<sup>1</sup>, and Takuya Nishimura<sup>2</sup>

*<sup>1</sup>U.S. Geological Survey  
345 Middlefield Rd., MS 977  
Menlo Park, CA 94025  
U.S.A.*

*<sup>2</sup>Geographical Survey Institute  
Geography and Crustal Dynamics Research Center  
Tsukuba, Japan*

Revised Version  
*J. Geophys. Res.*  
May, 2005

## **Abstract**

The slip distribution associated with the 1923  $M=7.9$  Kanto, Japan earthquake is re-examined in light of new data and modeling. We utilize a combination of first order triangulation, second order triangulation, and leveling data in order to constrain the coseismic deformation. The second order triangulation data, which have not been utilized in previous studies of 1923 coseismic deformation, are associated with only slightly smaller errors than the first order triangulation data and expand the available triangulation dataset by about a factor of 10. Interpretation of this data in terms of uniform slip models in a companion study (Nyst et al., 2005) shows that a model involving uniform coseismic slip on two distinct rupture planes explains the data very well and matches or exceeds the fit obtained by previous studies, even one which involved distributed slip. Using the geometry of the Nyst et al. (2005) 2-plane slip model, we perform inversions of the same geodetic dataset for distributed slip. Our preferred model of distributed slip on the Philippine Sea plate interface has a moment magnitude of 7.86. We find slip maxima of  $\sim 8$  to 9 meters beneath Odawara and  $\sim 7$  to 8 meters beneath the Miura peninsula, with a roughly 2:1 ratio of strike-slip to dip-slip motion, in agreement with a previous study (Wald and Somerville, 1995). However the Miura slip maximum is imaged as a more broadly-extended feature in our study, with the high-slip region continuing from the Miura peninsula to the southern Boso peninsula region. The second order triangulation data provide good evidence for  $\sim 3$  meters right-lateral strike slip on a 35-km long splay structure occupying the volume between the upper surface of the descending Philippine Sea plate and the southern Boso peninsula.

## **1 Introduction**

The 1923  $M=7.9$  Kanto, Japan earthquake devastated the major cities of Tokyo and Yokohama and caused more than 140,000 deaths. It occurred at a complex junction of the Philippine Sea (PHS), Pacific, and Honshu/North American plates (Figure 1), rupturing the dipping subducting plate interface between the PHS and Honshu plates along the Sagami trough. With a slip of about 7 meters (Kanamori, 1971; Ando, 1971, 1974) and a slip accumulation rate of 3 to 4 cm/yr (Yoshioka et al., 1994), the earthquake released about 200 to 300 years worth of accumulated tectonic

strain. Understanding the detailed mechanism of coseismic deformation associated with the earthquake is critical for understanding the budget of slip accumulation along the PHS-Honshu plate boundary and the resultant seismic hazard for the region.

Coseismic slip models for the Kanto earthquake have been presented by several previous authors. Kanamori (1971) used seismic surface wave data and P-wave focal mechanisms to infer the moment and slip geometry of the earthquake. He showed a model of a single rupture plane, with a combination of  $\sim 4$  m right-lateral strike-slip motion and  $\sim 2$  m dip-slip motion, adequately fit the considered seismic data. This rupture plane dips  $34^\circ$  towards the NE and coincides approximately with the PHS-Honshu plate interface. Ando (1971) used coseismic horizontal displacement field, as derived from first order triangulation data, and presented arguments that the fault plane ruptured the trace of the Sagami trough axis, implying that the upper edge of the coseismic rupture surface must have been located along this axis. This resulted in a "geodetic model" substantially different from that of Kanamori. Ando (1974) refined the interpretation of the same geodetic dataset considered by Ando (1971), with the aim of obtaining a coseismic slip model that was further consistent with supplementary information (triggering of magma movements beneath Oshima Island; triggering of secondary surface faulting; strong ground motion damage; marine terrace heights around Tokyo Bay and other geomorphological information). Matsu'ura et al. (1980) presented three new coseismic slip models and was the first study to have performed an inversion of coseismic deformation data for both the geometry and slip of one (or two) coseismic rupture planes. Wald and Somerville (1995) adopted the rupture plane obtained in Model I of Matsu'ura et al. (1980) and utilized a combination of seismic waveform data, a coseismic displacement field derived from first order triangulation data, and leveling data to derive a model of distributed slip (in both the right-lateral and dip-slip sense). They found local slip maxima of  $\sim 6 - 7$  m located beneath Odawara and the Miura peninsula (Figure 2).

With the exception of Wald and Somerville (1995), all of the above studies presented models of uniform slip on one or two coseismic rupture planes. Nyst et al. (2005, hereafter N05) compared the performance of these models based on their respective fits to a newly assembled coseismic dataset consisting of first and second order triangulation and leveling data. Among the models, Model III of Matsu'ura et al. (1980), which involves uniform slip on two rupture planes, fits the data as well or

better than the other models, including the distributed slip model of Wald and Somerville (1995). In particular, the 2-plane model of Matsu'ura et al. (1980) explains the dataset much better than any 1-plane model. The geodetic dataset analyzed in N05 includes first and second order triangulation data and leveling data. The analysis was performed on the triangulation data directly and not on a product (such as a displacement field derived from it). N05 performed grid searches for optimal 1-plane and 2-plane models (assuming uniform slip on each fault plane) that best explained this dataset. N05 found the best-performing model to be a 2-plane uniform-slip model that is very similar in geometry, slip sense, and magnitude to that of Matsu'ura et al. (1980, Model III), but with a significantly better fit.

The objective of this paper is to derive a distributed slip model for the 1923 earthquake. We use the identical triangulation and leveling dataset as N05 and consider two rupture surfaces that follow the 2-plane model of N05. We invert this dataset for the distribution of coseismic strike-slip and dip-slip motion on these rupture planes. We find that the distribution of slip on these rupture planes is concentrated in areas very close to the smaller uniform slip planes obtained in N05, and that it bears close similarity with the distributed slip model of Wald and Somerville (1995), though with notable differences. Finally we consider other aspects of the seismotectonics of the region in order to explore the possibilities of distributed slip on alternative PHS rupture surfaces and slip on faults not necessarily associated with the PHS-Honshu slab interface.

## **2 Dataset**

The dataset used here is identical to that used by N05. That study provides a detailed description of the dataset which we summarize briefly here. We utilize a combination of first order and second order triangulation data and leveling data, all of which was provided by the Geographical Survey Institute of Japan. The distributions of triangulation and leveling sites that contribute useful data are shown in Figure 3. In the first order triangulation dataset there are 31 included angles from 15 Kanto-area benchmarks with repeated pre-1923 and post-1923 measurements which cover the periods 1890-1898 and 1924/11-1927, respectively. In the second order triangulation dataset, there are 435 included angles from 178 Kanto-area benchmarks with repeated pre-1923 and post-1923 measurements from 1891 to 1927. The leveling data used

here consist of 8 routes with a total of 469 benchmarks. (A ninth route covering Izu Peninsula is displayed but not used in the modeling because its deformation is contaminated by volcanic processes.) Pre-1923 measurements were conducted from 1883 to 1898, and post-1923 measurements from 1923/10 to 1925.

Coseismic angle changes are typically 10 – 30 arcsec with apertures of several 10s of km, indicating coseismic horizontal strain changes of order  $\sim 50 - 150 \mu\text{strain}$ . The mean error associated with first order triangulation measurements, as obtained from triangle closure, is about 0.93 arcsec, and that associated with second order triangulation measurements is about 1.14 arcsec (N05). Thus the second order triangulation data is nearly as useful as the first order triangulation data and associated with about 10 times as many measurements. This data has not been considered previously in a study of 1923 coseismic slip.

Leveling data exhibits centers of 1.5 to 2 m subsidence around the southern Boso peninsula and the northern Sagami Bay near Odawara. The magnitude of geodetically-measured static deformation generally subsides towards the NE and reaches comparatively small levels around northern Sagami Bay. The raw leveling data consists of section height differences, but due to pervasive fluctuations in section height measurements along most lines, we find it preferable to work with the vertical displacement or accumulated section height differences. Summation of section height differences tends to result in a stable displacement curve in which slightly erratic movements of a few monuments are robustly averaged out. For a particular route, the displacement profile so obtained is without an absolute reference point and represents only the displacement relative to an arbitrary benchmark on the route. The error associated with the section height measurements is about  $0.5 - 0.6 \text{ mm}/\sqrt{\text{km}}$ . The resulting errors associated with vertical displacement then reaches only a few cm, which is much smaller than the tectonic signal (associated with coseismic rupture) and likely smaller than unmodeled signals due to source complexity or other processes.

Since the triangulation and leveling datasets include about 3 to 4 decades prior or subsequent to the 1923 earthquake, a corresponding amount of interseismic strain accumulation is contained in the observations. As in N05, we perform a correction of the overall dataset for interseismic loading using the interseismic strain accumulation model of Nishimura and Sagiya (2004). That model employs 34 dislocation planes to

develop a combined block and backslip model designed to match contemporary GPS and leveling observations. The magnitude of the correction is generally small (about 5-15% effect on an angle change and 5-10% effect on a leveling observation). Since the sense of interseismic strain accumulation is opposite to the sense of subsequent coseismic strain release, the impact of the correction is to slightly increase inferred coseismic slip.

### **3 Model of distributed slip**

#### **3.1 Choice of dislocation planes**

We aim to explain the coseismic geodetic dataset with a model of distributed slip on suitably defined rupture surfaces. As a first step we simplify the problem by choosing distinct dislocation planes on which to estimate distributed slip. Kanamori (1971) advocated a single rupture plane for the 1923 mainshock constrained by the focal mechanism solution and the seismically-determined locations of the mainshock and largest aftershocks; a single plane is remarkably consistent with the seismic information that he considered. Wald and Somerville (1995) also advocated a single rupture plane following Model I of Matsu'ura et al. (1980). However, N05 demonstrated the need for an additional plane with somewhat different geometry from the main coseismic rupture plane. The geometry of the N05 2-plane uniform slip model is shown by the black outlines in Figure 4. Single-fault models, which involve a fault plane that resembles the eastern fault plane of Figure 4, do not adequately explain either triangulation or leveling data in the vicinity of Odawara or the northern Izu peninsula. The western fault plane in Figure 4, which was derived jointly with the large plane, accomplishes the task of fitting these subsets of the dataset with a reasonable second dislocation plane, and the resulting 2-plane uniform slip model performs the best among all models considered by N05. From the point of view of fitting the geodetic data, the 2-plane uniform slip model of N05 is an excellent starting point. In order to test the possibility of slip outside the boundaries of these planes we extend the eastern plane by 20 km in the SE direction and extend the western plane by 5 km in both the NW and SE directions. The planes with these extensions are shown in gray in Figure 4.

### 3.2 Least squares inversion

We seek to obtain a model of distributed slip on selected dislocation planes that adequately explains the triangulation and leveling data. Let  $s_j(\hat{\mathbf{r}}')$  be the slip distribution in the  $j$ th slip sense at points  $\hat{\mathbf{r}}'$  located on the considered dislocation planes. On the larger dipping plane the rake is unconstrained, and we consider only shear dislocations involving right-lateral strike-slip motion ( $j=1$ ) or dip-slip motion ( $j=2$ ) on the larger plane. On the smaller plane we constrain the rake to be  $148^\circ$  as obtained in the  $30^\circ$ -dipping solution of N05. This defines a slip distribution ( $j=3$ ) on the smaller plane. Each slip distribution is represented within a local  $x$ - $y$  Cartesian coordinate system in terms of Hermite-Gauss (HG) functions:

$$s_j(x, y) = \sum_{p \geq 0}^{l_{\max}} \sum_{q \geq 0}^{l_{\max}} b_{jpq} h_p \left[ \frac{x}{L_1} \right] h_q \left[ \frac{y}{L_2} \right] \times \exp \left\{ -\frac{1}{2} \left[ \left[ \frac{x}{L_1} \right]^2 + \left[ \frac{y}{L_2} \right]^2 \right] \right\} \quad (1)$$

In equation (1), the functions  $h_p()$  are fully normalized Hermite polynomials, and  $L_1$  and  $L_2$  are length scales that are proportional to the dimensions of the particular plane. The HG functions are a convenient set of basis functions to use because they are mutually orthogonal, complete over  $(x, y)$  space, and they are localized in an easily controlled manner through appropriate choices of  $L_1$  and  $L_2$ . Each HG function generally tapers off to a relatively small value near the edges of the rectangular region. Let  $G_{mj}(\hat{\mathbf{r}}_i, \hat{\mathbf{r}}')$  be the Greens functions for  $m$ -component of displacement at  $\hat{\mathbf{r}}_i$  due to slip in  $j$ th slip sense at  $\hat{\mathbf{r}}'$ . The  $m$ -component of Cartesian displacement at site  $\hat{\mathbf{r}}_i$  is then

$$u_m(\hat{\mathbf{r}}_i) = \sum_j \int G_{mj}(\hat{\mathbf{r}}_i, \hat{\mathbf{r}}') s_j(\hat{\mathbf{r}}') d^2\hat{\mathbf{r}}' \quad (2)$$

To relate a theoretical angle change at included angle  $l$  to the triangulation benchmark displacements, we introduce transfer functions  $a_{iml}$  such that the  $l$ th angle change  $\Gamma_l$  has the form

$$\Gamma_l = \sum_m \sum_i a_{iml} u_m(\hat{\mathbf{r}}_i) \quad (3)$$

We use linearized least squares inversion theory to solve for the slip distribution. We seek to minimize a penalty function that is a combination of angle-change misfit and leveling-displacement misfit plus a roughness term, which is introduced in order to produce reasonably smooth slip distributions. The penalty function takes the form

$$\chi^2 = R \sum_k \sum_{i \in E_k} \left[ u_3(\hat{\mathbf{r}}_i) + c_k - d_i \right]^2 / \sigma_i^2 + \sum_l \left[ \Gamma_l - \gamma_l \right]^2 / \sigma_l^2 \quad (4)$$

$$+ S \sum_j \int \left| \nabla s_j(\hat{\mathbf{r}}') \right|^2 d^2 \hat{\mathbf{r}}'$$

where

$R$  = weighting factor for leveling data.

$k$  = leveling line index.

$E_k$  = set of sites belonging to leveling line # $k$ .

$d_i$  =  $i$ th leveling height change;  $\sigma_i$  = associated error.

$\gamma_l$  =  $l$ th angle change;  $\sigma_l$  = associated error.

$S$  = damping coefficient.

$c_k$  = reference height of  $k$ th leveling line.

The unknown model parameters that we seek to estimate are the HG coefficients of the slip distributions  $\{b_{jpq}\}$  and the reference heights of the leveling routes  $\{c_k\}$ . Denoting these model parameters by  $\{m_r\}$ , minimization of equation (4) leads to the normal equations

$$\sum_r \frac{1}{2} \left[ \frac{\partial^2}{\partial_q \partial_r} \chi^2 \right] \Big|_{(i)} m_r = - \frac{1}{2} \frac{\partial \chi^2}{\partial m_q} \Big|_{(i)} \quad (5)$$

where  $q$  and  $r$  span the set of model parameter indices, and the subscript  $(i)$  means that the derivatives are evaluated using initial values of  $m_r$  which are assumed zero. The Frechet derivatives (terms in parentheses in equation (5)) are determined straightforwardly from equation (4) and integral and recurrence relations among the HG functions. In particular, the contribution of the roughness term (that proportional to  $S$  in equation (5)) is given explicitly by equation (19) of Friederich and Wielandt (1995).

The Greens functions for the static response to point dislocation sources are calculated on a layered spherical Earth model (Figure 5). The parameters of this model are from Table 3 of Sato et al. (1998), and this model is considered an adequate representation of the regional elastic structure. The Greens functions are calculated in a spherical harmonic expansion using the method of Pollitz (1996).



### 3.3 Results

Referring to Figure 4, we perform inversions of the triangulation and leveling datasets for distributed coseismic slip on the two dipping planes plus uniform right-lateral slip on the vertical Boso transform fault. With  $l_{\max}=8$  in equation (1), there are a total of 135 slip parameters associated with the two dipping planes. There are 9 additional parameters  $\{c_k\}$  for the nine leveling routes. The inversions thus involve estimation of a total of 144 unknown parameters subject to a smoothness constraint on the slip distribution on the two dipping planes. This is controlled by the weight  $S$  in equation (4). Larger values of  $S$  result in smoother slip distributions but greater residual  $\chi^2$ . The appropriate value of  $S$  was chosen subjectively in order to balance the fit of the data with the need to obtain a smooth slip distribution with reasonable maximum amplitude.

The derived 1923 coseismic slip model is shown in Figure 6. It consists of combined right-lateral strike-slip motion and dip-slip motion on the two dipping planes, with strike-slip motion dominating. A sharp slip maximum of  $\sim 7 - 8$  m is located beneath Odawara and a much broader slip maximum of  $\sim 6 - 7$  m is located beneath the Miura peninsula, southern Tokyo Bay, and southern Boso peninsula. The predicted horizontal coseismic displacement field (Figure 7) shows maximum static offsets of  $\sim 5$  m on the Miura and southern Boso peninsulas. Displacement generally decreases towards the NE, in agreement with the general tendency of observed angle and height changes.

Predicted angle changes are compared with observed angle changes in Figure 8a-c. In Figure 8a,b the triangulation dataset has been subdivided into the angle changes derived from the first and second order triangulation data, and Figure 8c shows the fit to the composite dataset. The obtained fits are generally very good. However, while the amplitude of predicted horizontal strain agrees with the observed amplitude for the first order triangulation data, the amplitude is about 30% less than observed for the second order triangulation data. This is illustrated by the slope of the best-fitting straight line that relates the calculated and observed second order angle changes; the slope would be unity for a perfect fit but here is 1.27. Since the distribution of second order triangulation sites is roughly evenly interspersed with the first order sites (Figure 3 of N05), the source of the amplitude discrepancy is not immediately obvious. One

possibility is that an inherent horizontal to vertical discrepancy in the overall data set leads to an incompatibility in the first and second order triangulation data sets. We have tested whether this could be the case by downweighting the leveling data in the inversion, and the amplitude mismatch remains. We have also tested whether performing the interseismic loading correction could produce the mismatch; however, it is present regardless of whether the data are corrected for interseismic loading or not. The effect of the correction on the triangulation data is indicated in Figure 8d-f, which shows that the correction is small and does not substantially affect the amplitude of the triangulation observations. It may be related to the fact that the distances between second order triangulation sites are much smaller than distances between first order sites (Figure 3 of N05), so that sufficiently large areas that have strong gradients in horizontal strain would be fully represented with second order observations but somewhat smoothed out with first order observations. We explore the amplitude mismatch further in section 4.2.

Predicted height changes are compared with observed changes along the nine leveling routes in Figure 9. In areas where observed height changes were large, especially the Miura and Boso peninsulas, the agreement between modeled and observed changes is excellent. The only significant disagreement with observation occurs on the Izu peninsula route (Route F, which was not used in the modeling), and this is likely due to unmodeled volcanic processes on the peninsula, which is part of the Izu-Bonin volcanic arc.

The weight of leveling data  $R$  used in the slip inversion (equation (4)) has been chosen to balance the fits of both the leveling and triangulation datasets. The solid curves in Figure 10a show that triangulation misfit increases very slowly with increasing  $R$ , whereas leveling misfit decreases rapidly with increasing  $R$ . The slip inversion at the preferred value of  $R=0.42$  yields relatively low misfits in both datasets. Similarly, allowing for greater slip roughness (i.e., by decreasing the smoothing weight  $S$  in equation (4)) improves the fit of both the leveling and triangulation datasets, as shown by the solid curves in Figure 11a. Reasonable misfits are obtained at the chosen level of roughness, which is represented with a value of unity, corresponding to the black dots plotted on the solid curves in both Figure 10a and 11a.

## 4 Discussion

### 4.1 Model performance

The distributed 1923 coseismic slip model derived in the previous section has a seismic moment of  $6.92 \times 10^{20}$  Nm, corresponding to a moment magnitude  $M_w=7.86$ . It fits the data very well compared with previously published models. The fits of various coseismic slip models are compared in Figure 12. All models are measured against the triangulation and leveling datasets presented here and in N05, regardless of whether or not that data was used to derive a particular model. Comparison among these models demonstrates that the distributed slip model of this study performs the best in explaining the totality of the coseismic dataset. This result is not surprising given the many degrees of freedom available in the distributed slip model. An  $F$ -test may be applied to assess the significance of the improvement of fit of the distributed slip model relative to the 2-plane model of N05. The test function  $F$  depends on the NRMS of the two models being compared (Table 1), the number of independent data, and the number of degrees of freedom involved in the distributed slip inversion and the 2-plane uniform slip model of N05. The total number of independent triangulation and leveling measurements is 935 (N05). The number of degrees of freedom in the N05 model is 14. With  $l_{\max}=8$  and as discussed in section 3.3, we have 144 additional degrees of freedom in the inversion not used by N05. Putting this together with NRMS as shown in Figure 12, we find that  $F=1.76$ . This is a significant improvement in fit at the 99.999% confidence level.

Nevertheless, it is remarkable that the 2-plane model performs almost as well as the the distributed slip model of this study and better than the distributed slip model of Wald and Somerville (1995). This may reflect the fact that the two uniform slip planes determined by N05 (Figure 4), which are similar to the two uniform slip planes determined by Matsu'ura et al. (1980, Model III), coincide closely with the two moderate-maximum slip regions determined by Wald and Somerville (Figure 2) and this paper (Figure 6). This shows not only that the location of the principal slipping regions is robust among the various studies but also that the best fit to the data is achieved by oblique slip localized in two distinct regions, i.e., around Odawara and beneath the Miura peninsula.

The distributed slip model of this study yields the best fit to both the triangulation and leveling data sets. With respect to this data, we believe that it performs better than the Wald and Somerville (1995) model because our model accounts for the different fault geometry of the Odawara maximum relative to the Miura peninsula maximum, (i.e., the fault geometry of the large and small planes in Figure 4 are different), whereas the Wald and Somerville slip distribution is constrained to lie on a single fault plane. The need for more than one fault geometry was established in N05, where the 2-plane uniform slip model performs much better than the 1-plane uniform slip model (seen also in Figure 12). This advantage evidently carries over into the domain of distributed slip inversions and results in the overall excellent fit of our distributed slip model to the considered dataset.

#### **4.2 Model resolution**

How well we can resolve the details of slip is limited by the distribution and types of data. We performed resolution tests in order to assess how sensitive the dataset is to localized slip. Synthetic slip distributions in the strike-slip or dip-slip sense are generated on the larger dipping plane (Figure 4), then used to generate synthetic triangulation and leveling data. (Synthetic noise is not added.) This synthetic dataset is then inverted in the same manner as was the actual dataset. The results of the test are shown in Figure 13. Several localized slip maxima are put onto the eastern fault plane in either the strike-slip or dip-slip sense (top panels of Figure 13). The resulting slip distributions (bottom panels in Figure 13) are clearly a very smooth representation of the input slip distributions. The original strike-slip slip distribution is reproduced with smaller coherence than in the dip-slip case, likely because of the greater amount of constraints provided by leveling data relative to triangulation data on the Boso peninsula. The inverted slip in the dip-slip case not only recovers sharper features of the original slip distribution but also has good sensitivity to coseismic slip in the middle of the upper fault edge. There is comparatively little sensitivity to slip around the upper fault edge in the strike-slip case.

#### **4.3 Alternative distributed slip model**

The range of admissible models consistent with the geodetic data is fairly broad according to the parameter correlations presented in Figure 9 of N05. This motivates an inversion for a distributed slip model on alternative planes that possibly better account for the seismotectonics of the area. The strike of the eastern plane in the 2-plane solution of N05 is  $\sim 10^\circ$  counterclockwise of the axis of the Sagami trough. Ando (1971) presented several arguments regarding the likely rupture of the Sagami trough axis during the 1923 earthquake. Ando's observations would constrain the upper edge of the main rupture (i.e., the larger plane) to come to the surface along the Sagami trough, which strikes about  $314^\circ$ . The eastern fault plane chosen in this alternative model (Figure 14) therefore strikes  $314^\circ$ , has upper edge at the Sagami trough axis, and dips  $24^\circ$  in order to match the approximate location of the PHS-Honshu plate interface as imaged by seismicity data (Ishida, 1992). Focal mechanism solutions of the mainshock, which nucleated in the area of the western plane, indicate a dip of  $34^\circ$  (Kanamori, 1971) or possibly  $42^\circ$  (Pollitz et al., 1996). A preliminary 2-plane uniform-slip model investigated in N05 estimated a dip of  $30^\circ$  for the smaller plane. This is closer to the Kanamori's estimate of  $34^\circ$ , and therefore we adopt the  $30^\circ$  solution for the alternative western plane (Figure 14). Overall, the two planes chosen in this alternative model are within the broad range of admissible 2-plane models considered in N05 (i.e., Figure 9 of N05).

In this model we also allow for possible slip along a proposed offshore strike-slip fault (Lallemant et al., 1996) termed the Boso transform fault (Figure 14). Its existence was proposed on the basis of submarine geomorphological evidence for several km of slip at rates averaging about 15 mm/yr during the Holocene. Pollitz et al. (1996), using a suite of uniform slip inversions on pre-defined dislocation planes, inferred more than 1 m right-lateral coseismic slip on this fault. We include it here in order to test the viability of slip on this fault using the present dataset and in the context of distributed slip on the other dislocation planes.

Through appropriate choices of leveling weight  $R$  and roughness  $S$  in equation (4) we derive a slip distribution with identical misfit for both triangulation and leveling datasets as the distributed slip model using the extended N05 planes. The slip distribution on the two alternative planes, including the Boso transform, is shown in Figure 15. This slip distribution shares the same features as that derived on the N05 planes, particularly the distinct slip maxima beneath Odawara and the Miura peninsula, with

the Miura maximum extending broadly toward the ESE and passing under the southern Boso peninsula. Inferred right-lateral slip on the Boso transform is relatively minor  $\sim 0.4$  m. Predicted and observed angle changes are compared in Figure 16. Note that the tendency for amplitude mismatch in the second order triangulation is similar to that seen in the results with the N05 geometry (i.e., Figure 8b), with observed angle changes systematically higher. The slope of the best-fitting line relating the observed and calculated second order angle changes and constrained to pass through the origin is  $1.31 \pm 0.01$  for the alternative model (Figure 16b) and  $1.27 \pm 0.01$  for the N05 model (Figure 8b). This suggests that differences between the N05 and alternative fault geometries do not play a large role in the ability to fit the overall triangulation dataset.

#### **4.4 Non-PHS rupture during 1923 earthquake sequence**

The remaining  $\sim 30\%$  amplitude mismatch between observed and calculated second order angle changes may arise from additional, unidentified dislocation sources that shape the coseismic deformation field. We explore this idea by postulating right-lateral strike slip on a hypothetical structure located around the Boso peninsula. We choose pure right-lateral strike slip because the leveling data are fit well by the previously considered slip distributions, and a strike-slip source is unlikely to substantially alter the leveling fit. We focus on the Boso peninsula region because it has a great preponderance of second order triangulation measurements and a paucity of first order triangulation measurements (Figure 3; Figure 3 of N05), so that a strike-slip source placed here will affect mainly the predicted movements of second order triangulation sites. By joint inversion for distributed slip on the two PHS fault planes plus uniform strike slip on the hypothetical source, we conduct a trial-and-error search covering hypothetical slip planes throughout the Boso peninsula under a variety of possible geometries; the leveling weight  $R$  and roughness  $S$  are kept constant in these slip inversions. Results of this search are the same regardless of whether the extended N05 planes or the alternative planes are used for the PHS slip distribution. Fault planes located in central or northern Boso peninsula are found to be unsatisfactory (inferred slip is left lateral and the fit to the triangulation dataset is not improved by any fault movements in these areas). We find the best additional plane to be the "Boso Splay" fault shown in Figure 14. It is 35 km long, dips  $80^\circ$  towards the NE, and has lower

and upper edge depths of 17 and 4 km, respectively. The inverted slip is  $2.67 \pm 0.08$  m or  $2.80 \pm 0.08$  m right-lateral slip when using the extended N05 planes or alternative planes, respectively. The corresponding slip distributions for these two cases are shown in Figure 17a-b. The amount of slip required on the eastern plane is clearly reduced compared with the previous case (Figures 6 and 13), especially above southernmost Boso peninsula. NRMS for these models are listed in Table 1. For both cases these values are significantly better than the values of 4.50 and 7.50, respectively, obtained for the previously considered models (Table 1); i.e., the improvement in fit obtained with the 9 additional fault parameters for the Boso Splay is significant at nearly the 100% confidence level. The comparison between calculated and observed angle changes in Figure 18 demonstrates that the amplitude mismatch for the second order triangulation data is reduced from 1.27 (Figure 8b) to 1.16 (Figure 18b) for the case of the extended N05 planes, and from 1.31 (Figure 16b) to 1.20 (Figure 18e) for the case of the alternative planes.

The location of the inferred fault plane may be independently checked by inspection of the observed coseismic strain field as constrained by the triangulation data. In order to generate a coseismic strain field, we formulate a simple inverse problem in which the observed first and second order angle changes (including correction for interseismic loading) are fit with optimally-determined horizontal displacement vectors at the triangulation sites. The unknowns in this problem are the two components of horizontal displacement at all triangulation sites. The north and east components of the displacement field are parameterized separately in terms of smooth basis functions. A set of HG functions are used for this purpose. Although it is well known that such a displacement field is indeterminate in terms of both rotational strain and dilatation, the problem is rendered tractable by simply imposing a smoothness constraint on the solution. After making a reasonable choice of smoothing parameter, the resulting triangulation-derived coseismic displacement field is shown in Figure 19a. The method of Shen et al. (1996) is used to convert this displacement field into a strain field, from which we extract the deviatoric strain field (Figure 19b). In the southern Boso peninsula, a local maximum shear strain in the sense of right-lateral shear on a WNW-striking subvertical plane is resolved precisely in the location of the new fault. Since this local maximum is located well away from the upper edge of the PHS-Honshu interplate boundary, it follows that a local structure, rather than distributed slip

on the interplate boundary, best explains this part of the strain pattern.

The existence of the Boso Splay fault and its utility in explaining a large part of the signal in the second order triangulation data are robust with respect to the choices of leveling weight  $R$  and smoothing weight  $S$  used in the slip inversions. The trade-offs of leveling and triangulation NRMS with  $R$  and  $S$  (or equivalently, slip roughness) are shown in Figures 10a and 11a, respectively. The fit of each dataset is improved significantly with the addition of the Boso Splay fault. The slope of the second order triangulation predictions is consistently reduced towards the ideal value of unity regardless of the value of  $R$  (Figure 10b) or roughness (Figure 11b). These figures further demonstrate that estimated right-lateral strike slip on the Boso Splay fault is between 2.5 and 3.0 m over a wide range of values of  $R$  and slip roughness.

The inferred fault is likely associated with splay faulting from the PHS-Honshu slab interface (Saito and Ito, 2002), which is expressed at the surface as mapped right-lateral strike-slip faults on the Boso and Miura peninsulas (Kaneko, 1972). These faults are associated with an ophiolitic body emplaced during the Miocene (Ogawa and Taniguchi, 1988). Gravity and magnetic data indicate that the ophiolitic body dips steeply towards the NE (Morijiri et al., 1987). Concerning uncertainties in the geometry of the Boso Splay plane, it is found that an upper edge depth less than 3 km results in a deterioration of NRMS as well as the slope of the calculated vs. observed angle changes for the second order triangulation data. The same is true if the fault plane is lengthened by more than 5 km in the NW direction or more than 10 km in the SE direction, or if the upper edge is moved northward or southward by more than 2 km. This suggests that regardless of the subsurface continuity of subvertical structures between the Boso and Miura peninsulas, the splay faulting associated with the 1923 Kanto earthquake likely involved only the part beneath the Boso peninsula and not that beneath the Miura peninsula. The inferred involvement of the Boso Splay in the 1923 Kanto earthquake is consistent with the occurrence of numerous large aftershocks located 300 – 350 km distant from Gifu (Takemura, 1994). These distant aftershocks occurred on the second day after the mainshock. If they are indeed associated with the Boso Splay, then they may have been triggered by the unclamping of this fault by the dip-slip faulting that occurred on the shallow part of the adjacent PHS-Honshu interface (Figure 17).



The seismic moment associated with distributed slip on the PHS interplate boundary using the extended N05 planes in combination with the Boso Splay is  $6.87 \times 10^{20}$  Nm, corresponding to  $M_w = 7.85$ . The additional moment contributed by the Boso Splay fault is  $3.35 \times 10^{19}$  Nm, corresponding to  $M_w = 6.98$ .

#### **4.5 Regional seismic hazard implications**

The distribution of slip carries important implications for estimated slip deficit in the region and resulting seismic hazards. Models of interseismic strain accumulation (e.g., Yoshioka et al., 1994; Henry et al., 2001; Sagiya, 2004; Nishimura and Sagiya, 2004) indicate how rapidly various sections of the PHS-Honshu and Pacific-Honshu plate interfaces are currently being loaded. The PHS-Honshu plate interface, while dominated by the subducting slab beneath Sagami Bay during the 1923 event, is overall very complicated because of the presence of offshore faults which are suspected to have been active in the past and are potentially important for future slip. This includes fault B of Matasuda et al., (1978), which likely ruptured during the great 1703 Genroku earthquake, and the northern and southern boundaries of a "Boso Sliver" advocated by Lallemand et al. (1996) and Pollitz et al. (1996). (Referring to Figure 1, the Boso sliver represents the block bounded by the Boso transform fault to the north and the Pacific extension of the Sagami trough to the south.) Matsuda et al.'s fault B apparently did not rupture in 1923 based on the lack of coseismic slip detected in this region (Wald and Somerville, 1995; Figure 6). The backslip model of interseismic strain accumulation of Nishimura and Sagiya (2004) does not account for fault B but hypothesizes that strain accumulation in the vicinity of the southern Boso peninsula is accommodated on the PHS-Honshu interface estimated by Ishida (1992). The resulting strain accumulation model yields about 3.9 cm/yr strain accumulation on the oceanward extension of the Sagami trough (planes #13 and 14 of Nishimura and Sagiya, 2004). This part of the PHS-Honshu subduction interface is located east of the Boso peninsula and probably did not rupture in 1923. Pollitz et al. (1996) suggest that Matsuda et al.'s fault C, which ruptured in the 1703 earthquake, should be part of the oceanward extension of the Sagami trough, i.e., along the southern boundary of the Boso sliver. The strain accumulation model of Nishimura and Sagiya (2004) would imply a present slip deficit of about 12 m on the subduction interface

east of the Boso peninsula, part or all of which may have ruptured in 1703. The Boso transform fault may possibly accommodate 1.6 cm/yr long-term right-lateral slip (Lallemant et al., 1990). If this slip rate is applicable to the splay faults that exist beneath the Boso and Miura peninsulas, and assuming that these faults did not slip between 1703 and 1923, then 2 m of potential slip may be presently stored on this fault if it slipped  $\sim 3$  m in the 1923 earthquake sequence.

## 5 Conclusions

The faulting mechanism of the 1923 Kanto earthquake is re-examined in order to refine the fault geometry and slip and account for data that was not included in previous studies of the coseismic deformation. We assemble available first order and second order triangulation data and leveling data and perform inversion of this geodetic dataset for the distribution of coseismic slip. Using the 2-plane uniform-slip model derived in Nyst et al. (2005), we allow for variable strike-slip and dip-slip motion on the principal coseismic rupture plane occupying the Sagami trough and oblique slip with fixed rake on a second rupture plane onland beneath Odawara. We find a sharp slip maximum of  $\sim 7 - 8$  m beneath Odawara and a much broader slip maximum of  $\sim 6 - 7$  m beneath the Miura peninsula, southern Tokyo Bay, and western Boso peninsula. A rake of about  $150^\circ$  is obtained consistently on the larger (eastern) coseismic rupture plane west of the Boso peninsula, indicating a roughly 2:1 ratio in strike-slip to dip-slip motion, in agreement with previous studies. The rake rotates to  $135^\circ - 140^\circ$  around the southern Boso peninsula, indicating more dip-slip motion on the PHS-Honshu interface here than elsewhere. This result is obtained for slip distributions estimated on the extended Nyst et al. (2005) fault planes as well as alternative fault planes modified by independent seismotectonic information. Overall, the coseismic slip direction of the footwall of the principal coseismic rupture planes is a few degrees clockwise of the present PHS-Honshu plate convergence direction as inferred by recent geodetic data (Yoshioka et al., 1994; Mazzotti et al., 2001; Sagiya et al., 2004), suggesting a degree of slip partitioning along the complicated plate boundary. The areas of moderate to high slip coincide well with the uniform slip planes in the 2-plane model determined in Nyst et al. (2005) as well as Matsu'ura et al. (1980) Model III, the distributed slip model of Wald and Somerville (1995), and an alternative distributed slip model presented here, showing that the regions of inferred

relatively high coseismic slip are robust among the various studies.

The second order triangulation dataset, which is ten times larger than the first order triangulation dataset considered in previous studies, is difficult to explain with a model of distributed slip on the PHS-Honshu slab interface alone. In order to explain this dataset in detail we infer ~3 m right-lateral strike slip on a ~35-km long, subvertical fault beneath the southern Boso peninsula. This fault is interpreted as a splay structure between the descending PHS plate and the Boso peninsula and projects to the surface along mapped active faults. Its involvement in the 1923 Kanto earthquake may help explain slip partitioning between the slab interface and crustal faults in accommodating the PHS-Honshu relative plate motion.

*Acknowledgments.* We are grateful to Shinji Toda, Takeshi Sagiya, Wayne Thatcher and Ross Stein for helpful discussions. This paper was improved by internal reviews by Ruth Harris and Jim Savage and comments by two anonymous reviewers and the Associate Editor.

## References

- Ando, M., A fault-origin model of the Great Kanto earthquake of 1923 as deduced from geodetic data, *Bull. Earthq. Res. Inst.*, 49, 19-32, 1971.
- Ando, M., Seismo-tectonics of the 1923 Kanto earthquake, *J. Phys. Earth*, 22, 263-277, 1974.
- Friederich, W., and E. Wielandt, Interpretation of seismic surface waves in regional networks: joint estimation of wavefield geometry and local phase velocity -- method and tests, *Geophys. J. Int.*, 120, 731-744, 1995.
- Henry, P., S. Mazzotti, and X. LePichon, Transient and permanent deformation of central Japan estimated by GPS, 1. Interseismic loading and subduction kinematics, *Earth Planet Sci. Lett.*, 184, 443-453, 2001.
- Ishida, M., Geometry and relative motion of the Philippine Sea plate and Pacific plate beneath the Kanto-Tokai district, Japan, *J. Geophys. Res.*, 97, 489-513, 1992.
- Kanamori, H., Faulting of the Great Kanto earthquake of 1923 as revealed by seismological data, *Bull. Earthq. Res. Inst.*, 49, 13-18, 1971.
- Kaneko, S., Some remarks on the strike-slip faulting in Miura peninsula And Sagami bay area, south Kanto, Japan, *J. Geol. Soc. Japan*, 78, 203-212, 1972.
- Lallemant, S., X. Le Pichon, F. Thoue, and P. Henry, Shear partitioning near the central Japan triple junction: the 1923 great Kanto earthquake revisited -- I, *Geophys. J. Int.*, 126, 871-881, 1996.
- Matsu'ura, T. Iwasaki, Y. Suzuki, and R. Sato, Statical and dynamical study on faulting mechanism of the 1923 Kanto earthquake, *J. Phys. Earth*, 28, 119-143, 1980.
- Mazzotti, S., P. Henry, X. LePichon, Transient and permanent deformation of central Japan estimated by GPS 2. Strain partitioning and arc-arc collision, *Earth Planet Sci. Lett.*, 184, 455-469, 2001.
- Morijiri, R., H. Kinoshita, and T. Nago, On the geophysical survey of the Mineoka ophiolite belt, southern part of Boso peninsula, Chiba prefecture, Japan, *Ann. Rep. Inst. Mar. Ecosystem, Chiba University*, 7, 24-26, 1987.
- Nishimura, T., and T. Sagiya, Crustal block kinematics around the northernmost Philippine Sea plate, central Japan estimated from GPS and Leveling data, *J. Geophys. Res.*, submitted, 2004.
- Nyst, M., T. Nishimura, N. Hamada, F.F. Pollitz, and W. Thatcher, The 1923 Kanto

- earthquake re-evaluated using a newly augmented geodetic data set, *J. Geophys. Res.*, *submitted*, 2005.
- Ogawa, Y., and H. Taniguchi, Geology and tectonics of the Miura-Boso Peninsulas And the adjacent area, *Modern Geology*, *12*, 147-168, 1988.
- Pollitz, F.F., X. LePichon, and S.J. Lallemand, Shear partitioning near the central Japan triple junction: the 1923 great Kanto earthquake revisited -- II, *Geophys. J. Int.*, *126*, 882-892, 1996.
- Pollitz, F.F., Coseismic deformation from earthquake faulting on a layered spherical Earth, *Geophys. J. Int.*, *125*, 1-14, 1996.
- Sagiya, T., Interplate coupling in the Kanto district, central Japan, and the Boso peninsula silent earthquake in May 1996, *Pure Appl. Geophys.*, in press, 2004.
- Saito, T., and M. Ito, Deposition of sheet-like turbidite packages and migration of channel-overbank systems on a sandy submarine fan: An example from the late Miocene-Early Pliocene forearc basin, Boso Peninsula, Japan, *Sedimentary Geology*, *149*, 265-277, 2002.
- Sato, T., R.W. Graves, P.G. Somerville, and S. Kataoka, Estimates of regional and local strong motions during the Great 1923 Kanto, Japan, earthquake (Ms 8.2). Part 2: Forward simulation of seismograms using variable-slip rupture models and estimation of near-fault long-period ground motions, *Bull. Seismol. Soc. Am.*, *88*, 206-227, 1998.
- Shen, Z.-K., D.D. Jackson, and B.X. Ge, Crustal deformation across and beyond the Los Angeles basin from geodetic measurements, *J. Geophys. Res.*, *101*, 27,957-27,980, 1996.
- Takemura, M., Aftershock activities of two days after the 1923 Kanto earthquake (M=7.9) inferred from seismograms at Gifu Observatory, *Zishin*, *46*, 439-445, 1994 (in Japanese).
- Wald, D.J., and P.G. Somerville, Variable-slip rupture model of the great 1923 Kanto, Japan, Earthquake: geodetic and body-waveform analysis, *Bull. Seism. Soc. am.*, *85*, 159-177, 1995.
- Yoshioka, S., T. Yabuki, T. Sagiya, T. Tada, and M. Matsu'ura, Interplate coupling in the Kanto district, central Japan, deduced from geodetic data inversion and its tectonic implications, *Tectonophysics*, *229*, 181-200, 1994.

## Figure Captions

Figure 1. Tectonic setting of the Kanto and Tokai, Japan districts indicating major tectonic boundaries. PHS=Philippine Sea plate; PAC=Pacific plate; Honshu/N.AMER=Honshu/North American plate; AMUR=Amurian plate; ISTL=Itoigawa-Shizuoka Tectonic Line.

Figure 2. Variable slip model of Wald and Somerville (1995). Top panel shows the dipping fault plane used in their study, which is the Kanamori (1971) fault plane. The middle and lower panels show the distributions of slip amplitude and direction, respectively.

Figure 3. Distribution of first and second order triangulation sites and leveling sites used in this study. Note the much greater number of second order triangulation sites compared with first order triangulation sites.

Figure 4. (Black outlines) Fault geometry and slip of the best 2-plane uniform slip model determined in Nyst et al. (2004). Both planes dip  $27^\circ$  towards the NE and have an upper edge depth of 3 km. The larger plane has lower edge depth of 27 km, and the smaller plane has lower edge depth of 32 km. Slip amplitudes and uncertainties associated with each plane are indicated. (Two gray planes) Extensions of the Nyst et al. (2004) planes on which we derive a distributed slip model.

Figure 5. Depth distribution of elastic moduli used to describe the layered elastic structure (prescribed by the "HNG" entries of Table 3 of Sato et al., 1998).

Figure 6. Distributed slip model of 1923 coseismic rupture. The color scale indicates the amplitude of slip and the arrows the direction of movement of the hanging wall. Variable rake is allowed for the larger (eastern) plane, while the rake is fixed at  $145^\circ$  on the smaller plane.

Figure 7. The horizontal static displacement field produced by the slip distribution of Figure 6 and the layered Earth structure of Figure 5.

Figure 8. Comparison of observed and calculated angle changes for first order triangulation (a), second order triangulation (b), and the combined triangulation dataset (c). Calculated angle changes are for the distributed slip model on the

N05 fault planes. Comparison of angle changes corrected/uncorrected for interseismic strain accumulation (prescribed by the Nishimura et al., 2004 model) for first order triangulation (d), second order triangulation (e), and the combined triangulation dataset (f).

Figure 9. Comparison of observed leveling displacements (points with error bars denoting one standard deviation) and calculated coseismic uplift (dashed lines) on the nine indicated leveling routes. On these routes are indicated the origin of the leveling profile and (for profiles B, D, and F) the sense of traverse.

Figure 10. (a) Dependence of leveling and triangulation NMRS on leveling weight  $R$  for a fixed value of slip smoothing weight, i.e., the value of  $S$  used in the preferred slip models. Results are shown separately for the inversions without the Boso Splay fault (solid curves) and with the Boso Splay fault (dashed curves). Black dots indicate the NRMS obtained at the preferred value of  $R$ . (b) The slope of the best-fitting line in the second order triangulation predicted versus observed angle changes (as in Figure 8b) is shown as a function of leveling weight  $R$ . Separate slopes are shown for the cases of inversion without the Boso Splay fault (solid curves) and with the Boso Splay fault (dashed curves). For the latter set of inversions, the corresponding right-lateral strike slip estimated on the Boso splay fault is shown. Black dots indicate the values of slope and slip obtained at the preferred value of  $R$ .

Figure 11. (a) Dependence of leveling and triangulation NMRS on slip roughness, which is controlled by the choice of slip smoothing weight  $S$ , for a fixed value of leveling weight, i.e., the value of  $R$  used in the preferred slip models. Results are shown separately for the inversions without the Boso Splay fault (solid curves) and with the Boso Splay fault (dashed curves). Black dots indicate the NRMS obtained at the preferred value of  $S$ . (b) The slope of the best-fitting line in the second order triangulation predicted versus observed angle changes (as in Figure 8b) is shown as a function of slip roughness. Separate slopes are shown for the cases of inversion without the Boso Splay fault (solid curves) and with the Boso Splay fault (dashed curves). For the latter set of inversions, the corresponding right-lateral strike slip estimated on the Boso splay fault is shown.

Black dots indicate the values of slope and slip obtained at the preferred value of  $S$ .

Figure 12. Normalized misfit (reduced chi squared) of selected coseismic slip models with respect to the triangulation and leveling datasets used in this study. The predictions of each model are compared with the present dataset regardless of whether or not parts of our dataset were used to derive the given model.

Figure 13. Resolution tests for coseismic dip-slip and strike-slip motion on the larger rupture plane. Synthetic data are generated using the indicated synthetic slip distributions (top panels) and inverted in exactly the same manner as the actual data. The inverted slip distributions (lower panels) are much smoother than the input slip distributions because of the effect of minimizing the slip roughness in the inversion.

Figure 14. Geometry of coseismic rupture planes used to derive alternative slip models. The two dipping planes are modified from the Nyst et al. (2005) 2-plane geometry using seismotectonic information. The larger plane has length 75 km and strike  $314^\circ$ . The smaller plane has length 34 km and strike  $290^\circ$ . Following Lallemand et al. (1996), the Boso transform is assumed to be a vertical right-lateral strike-slip fault with uniform slip. The "Boso Splay" is a hypothesized fault plane dipping  $80^\circ$  to the NE associated with splay faulting from the NE-dipping PHS-Honshu interface. This fault plane has lower and upper edge depths of 17 km and 4 km, respectively, and is assumed to slip with pure right-lateral strike slip.

Figure 15. Distributed slip model of 1923 coseismic rupture obtained by inversion for slip on two alternative PHS fault planes plus uniform right-lateral slip on the Boso transform. The color scale indicates the amplitude of slip and the arrows the direction of movement of the hanging wall. Variable rake is allowed for the larger (eastern) plane, while the rake is fixed at  $148^\circ$  on the smaller plane.

Figure 16. Comparison of observed and calculated angle changes for first order triangulation (a), second order triangulation (b), and the combined triangulation dataset (c). Calculated angle changes are for the distributed slip model on the



two alternative fault planes plus uniform right-lateral slip on the Boso transform.

Figure 17. Distributed slip model of 1923 coseismic rupture obtained by inversion for slip on either the two extended N05 planes (a) or the two alternative PHS fault planes (b) plus right-lateral strike slip on the Boso Splay. The color scale indicates the amplitude of slip and the arrows the direction of movement of the hanging wall.

Figure 18. Comparison of observed and calculated angle changes for first order triangulation (a), second order triangulation (b), and the combined triangulation dataset (c). Calculated angle changes are for the distributed slip model on the two extended N05 fault planes plus right-lateral slip on the Boso Splay. (d, e, f) show the comparison for the case of the distributed slip model on the two alternative fault planes plus right-lateral slip on the Boso Splay.

Figure 19. Coseismic horizontal displacement field (a) and shear strain field (b) derived from the first and second order triangulation data. To represent the deviatoric strain field, we plot the orientations of the deviatoric principal strain axes with corresponding magnitudes  $e_1$  and  $e_2 = -e_1$ . The color scale depicts the quantity  $\frac{1}{2}(e_1 - e_2)$ .

<b>Table 1</b>					
Fit of distributed slip models					
	extended N05 planes	extended N05 planes + Boso Splay	Alternative planes + Boso transform	Alternative planes + Boso Splay	N05 2-plane uniform slip
NRMS <sup>a</sup>	4.50	4.37	4.50	4.44	5.10
NRMS <sup>b</sup>	7.50	7.32	7.50	7.29	8.80
<p><sup>a</sup> Normalized misfit for the triangulation dataset</p> <p><sup>b</sup> Normalized misfit for the leveling dataset</p> <p>All misfits are computed with equation (3) of Nyst et al. (2005).</p>					

Figure 1

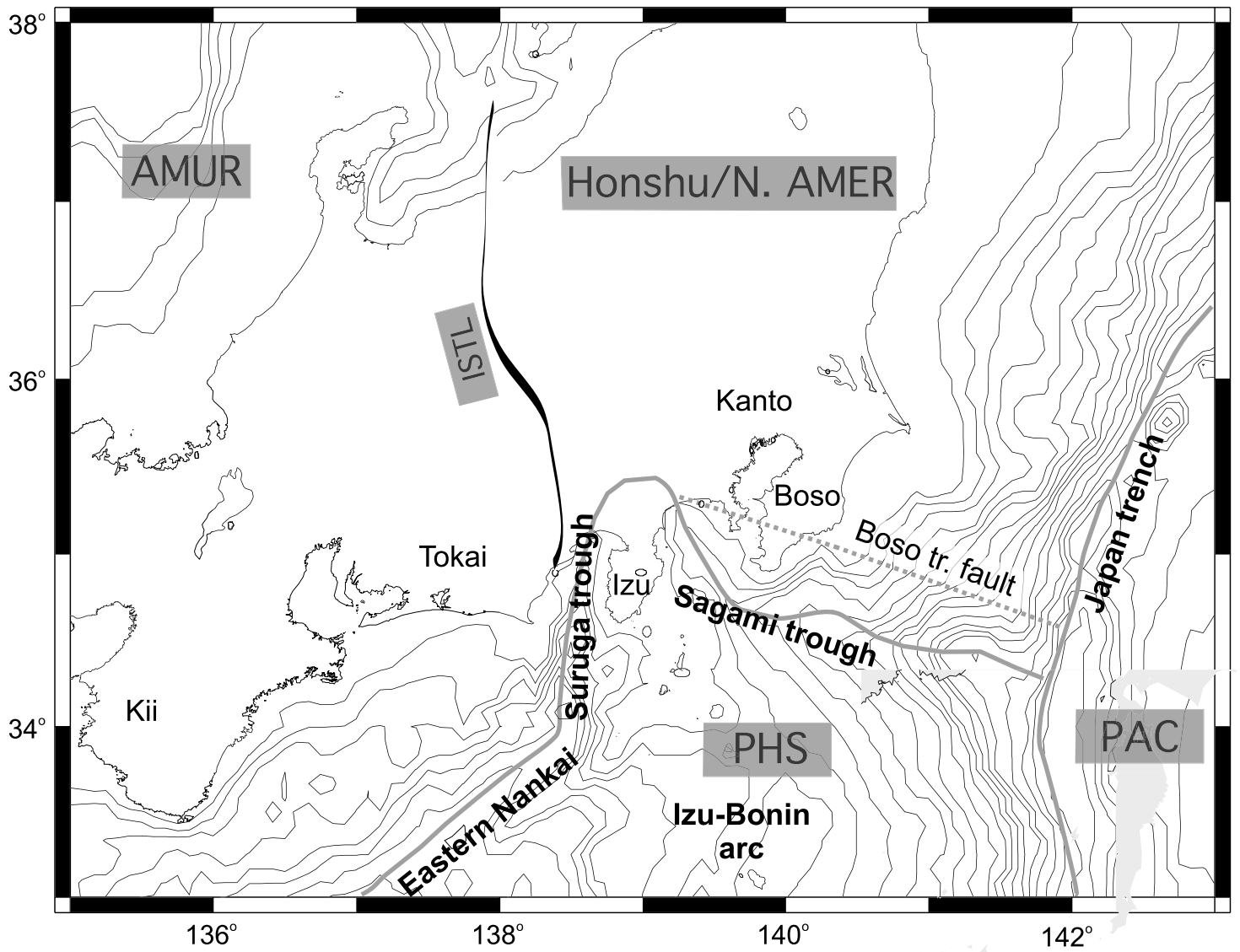
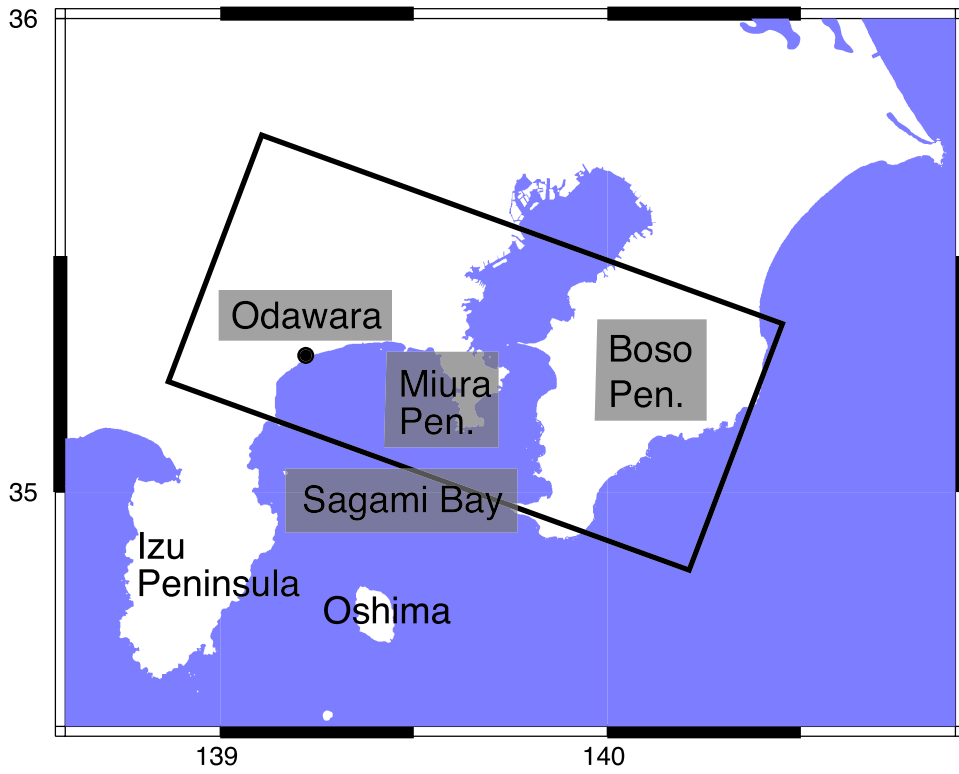


Figure 2



Contoured Slip Distribution

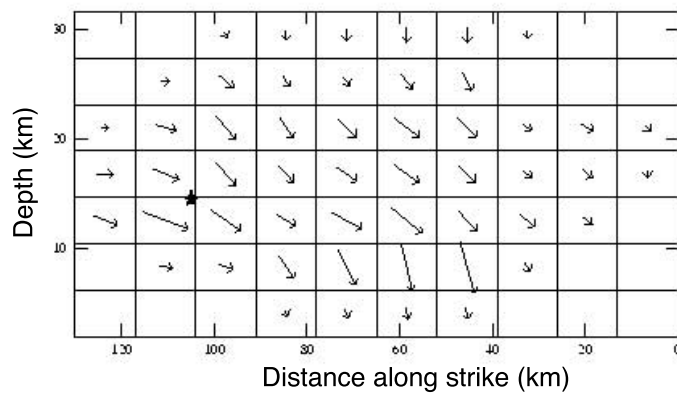
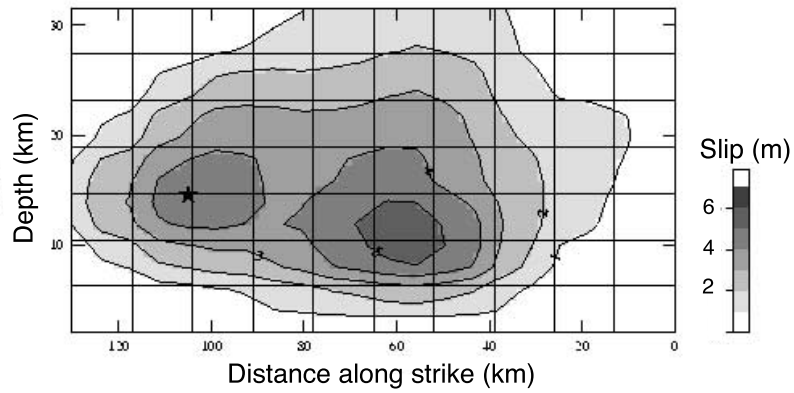


Figure 3

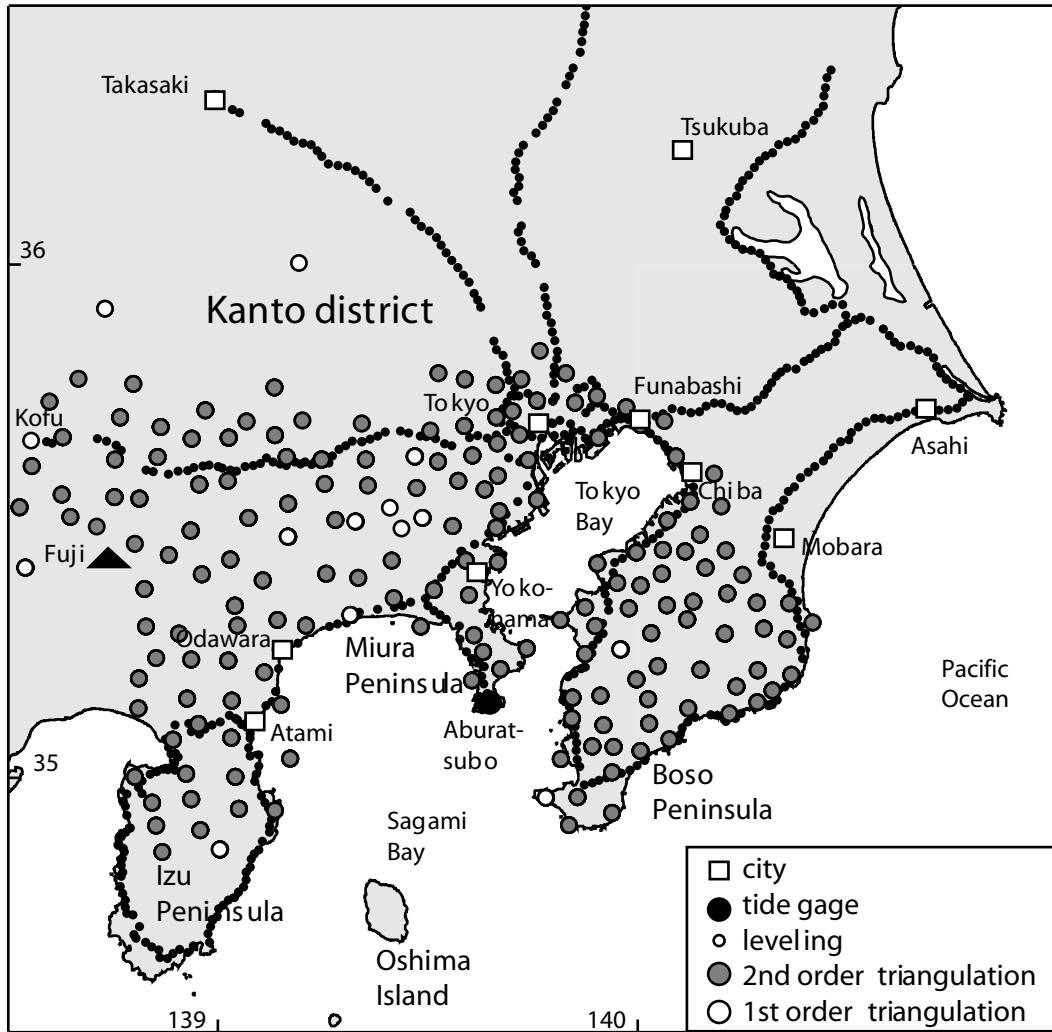


Figure 4

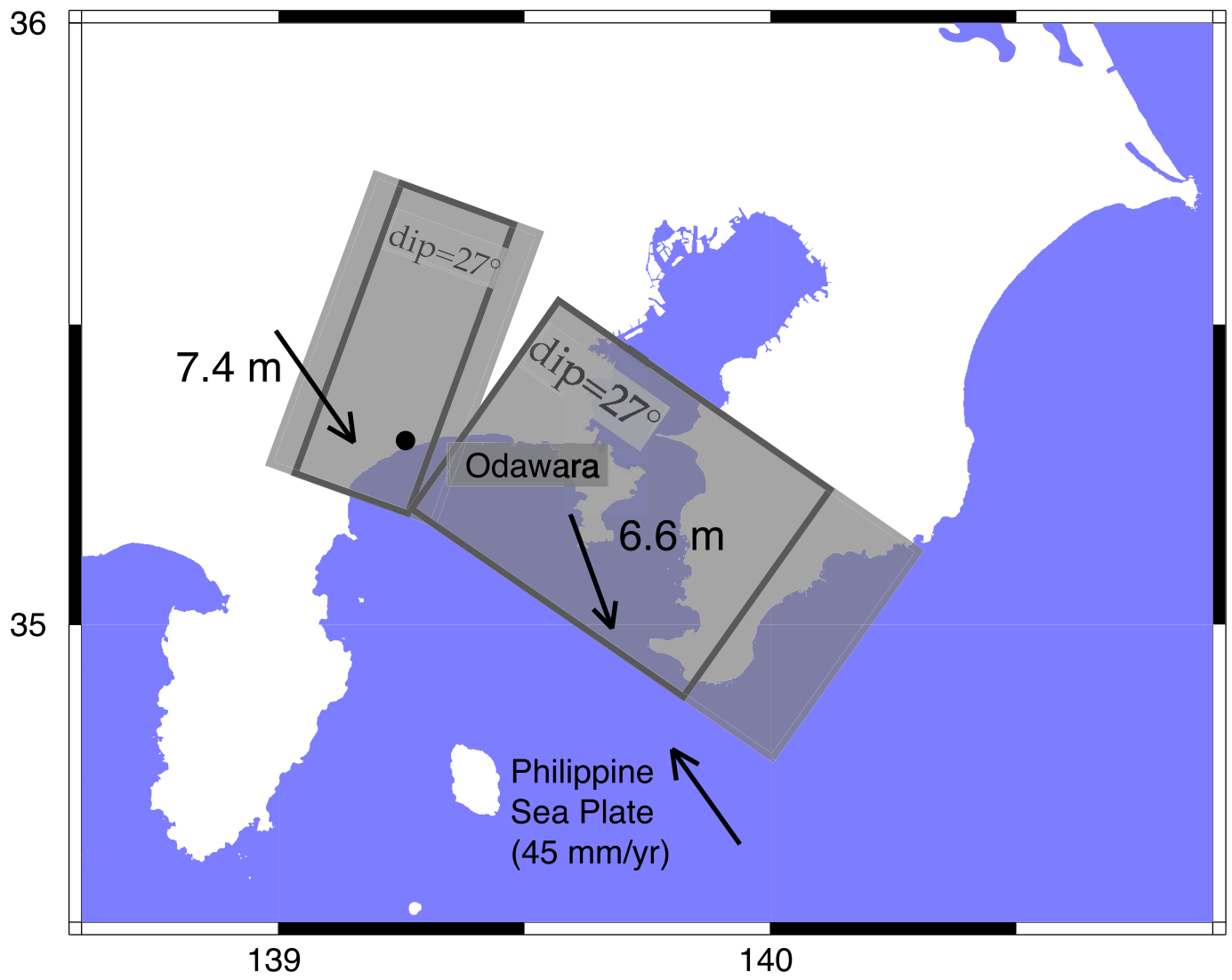
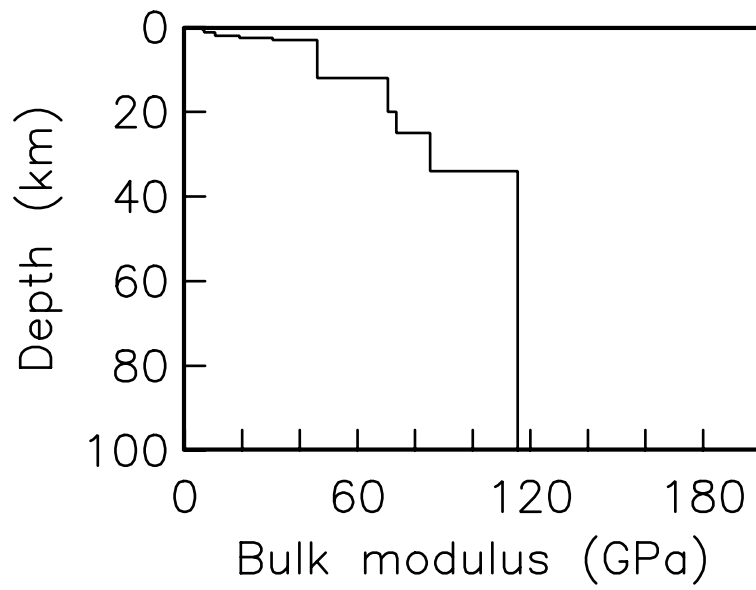
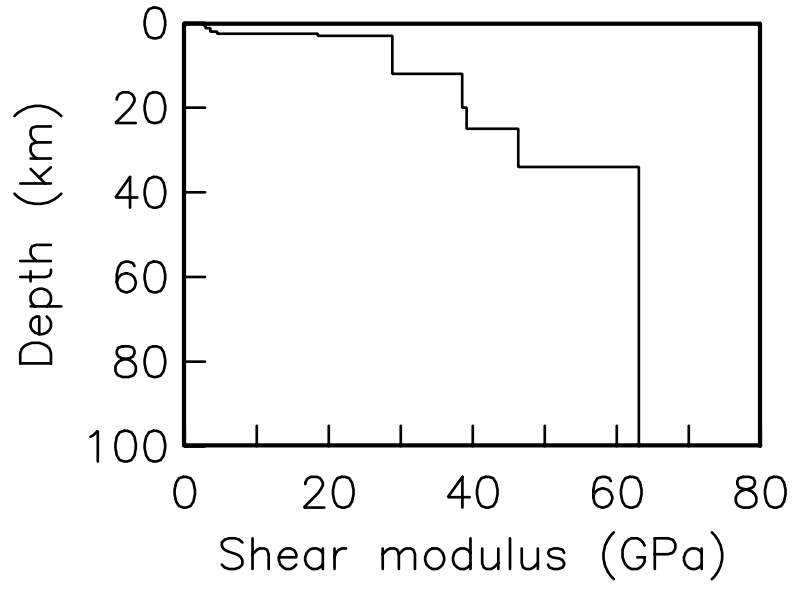
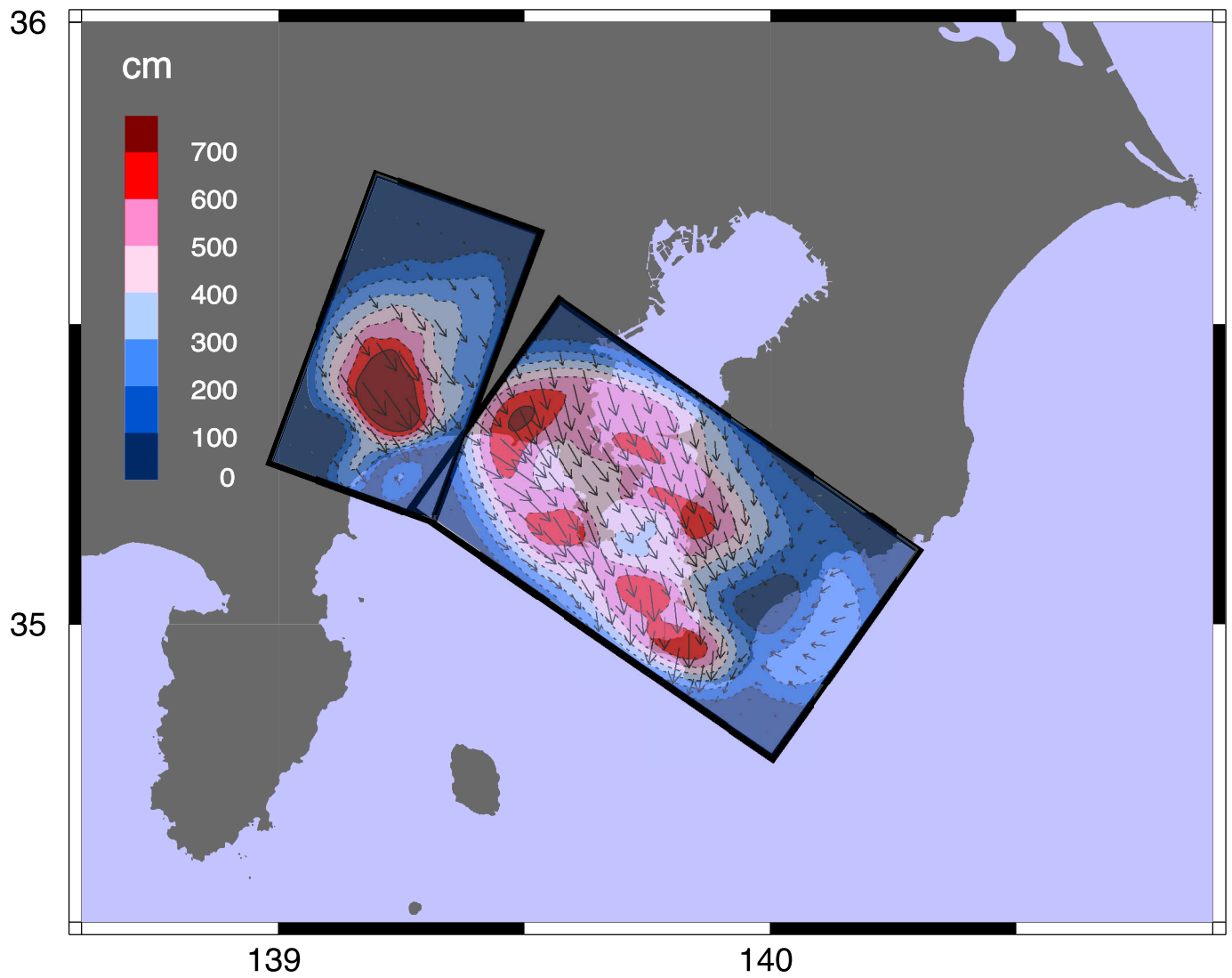


Figure 5



### Extended N05 planes





### Coseismic Displacement Field

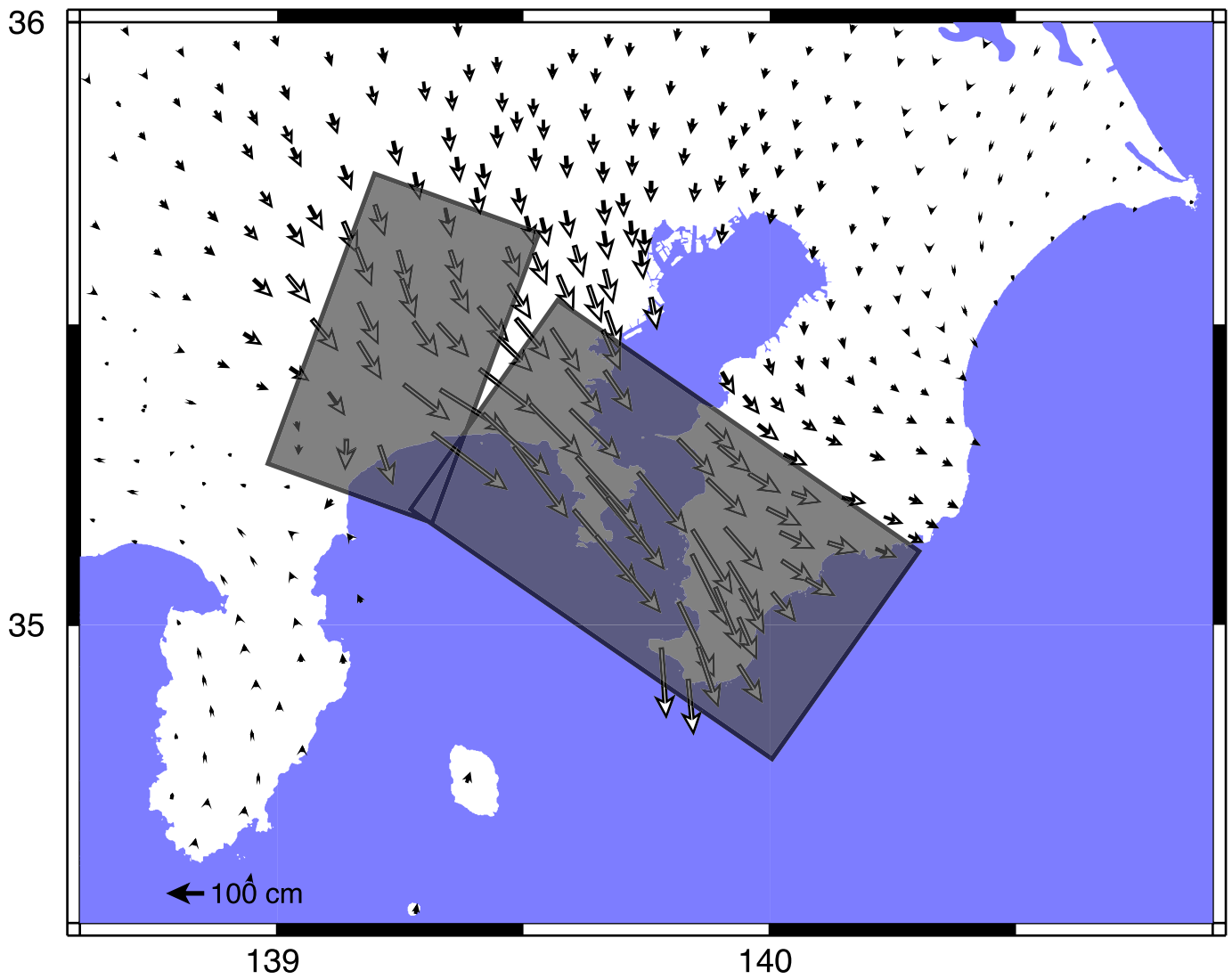


Figure 8

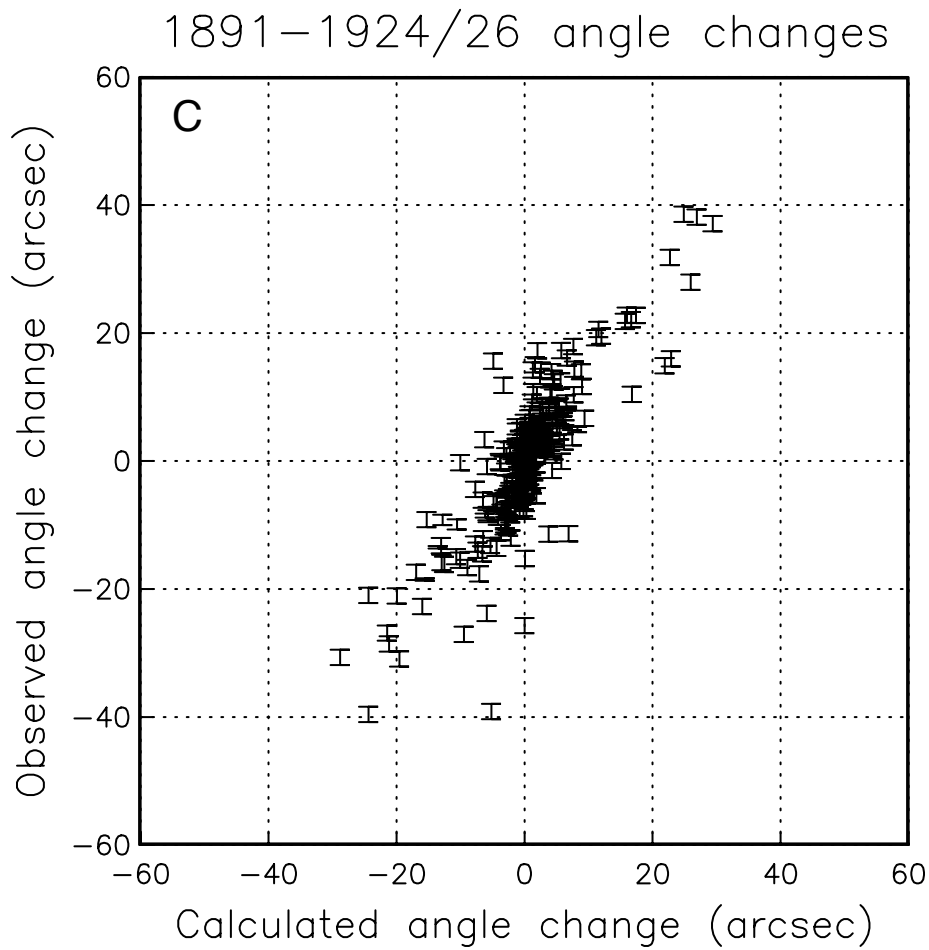
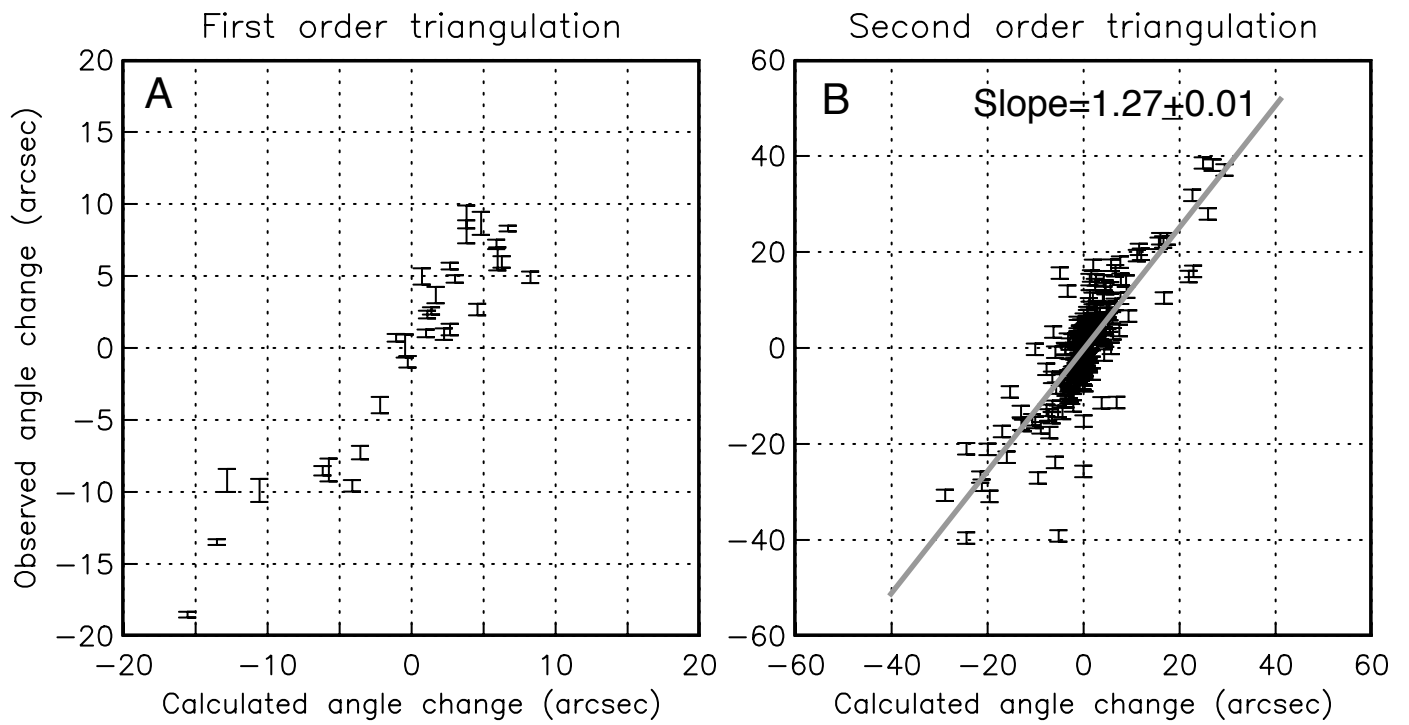


Figure 8

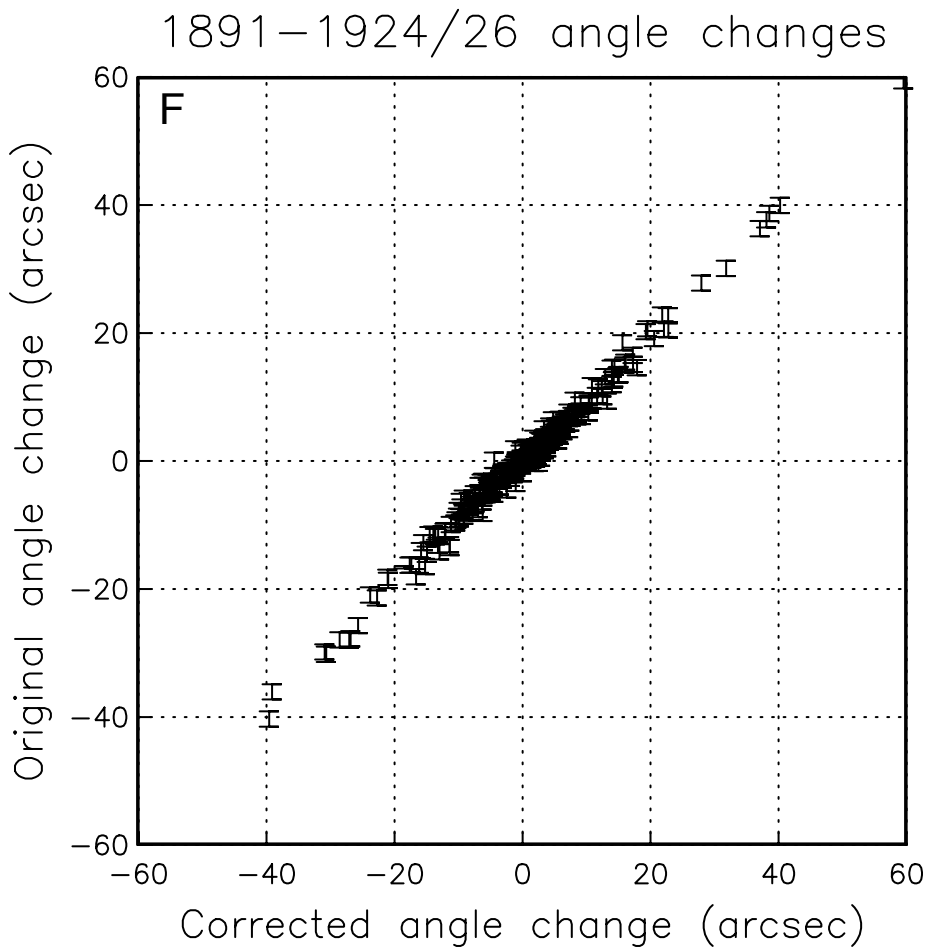
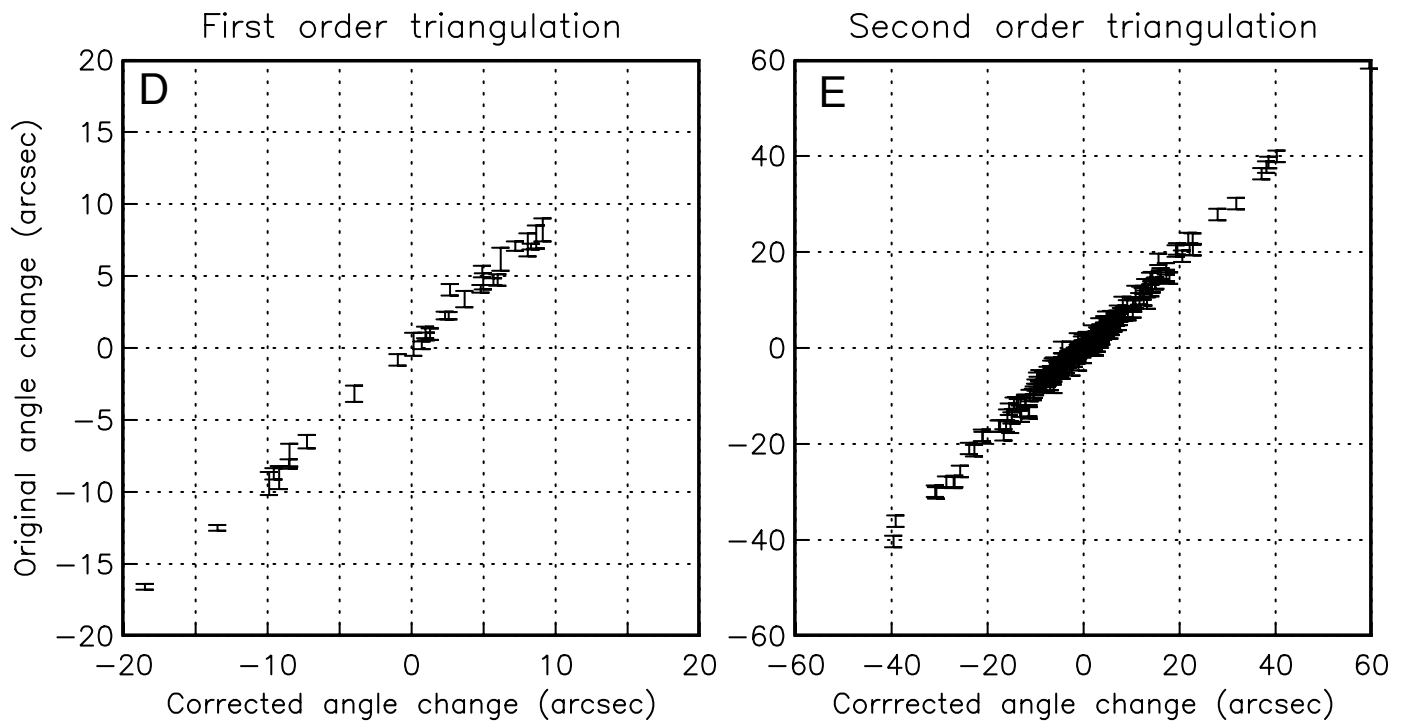
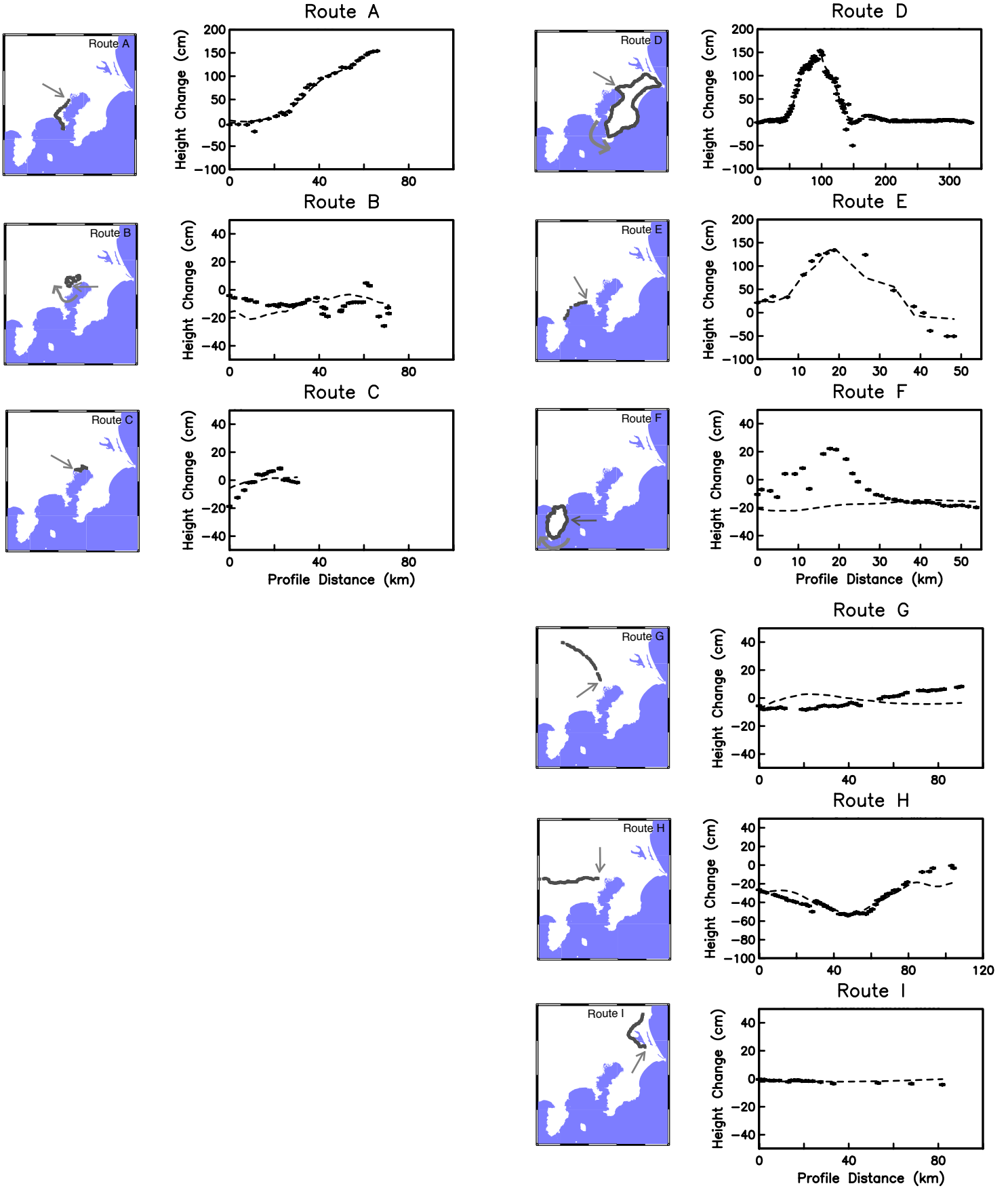
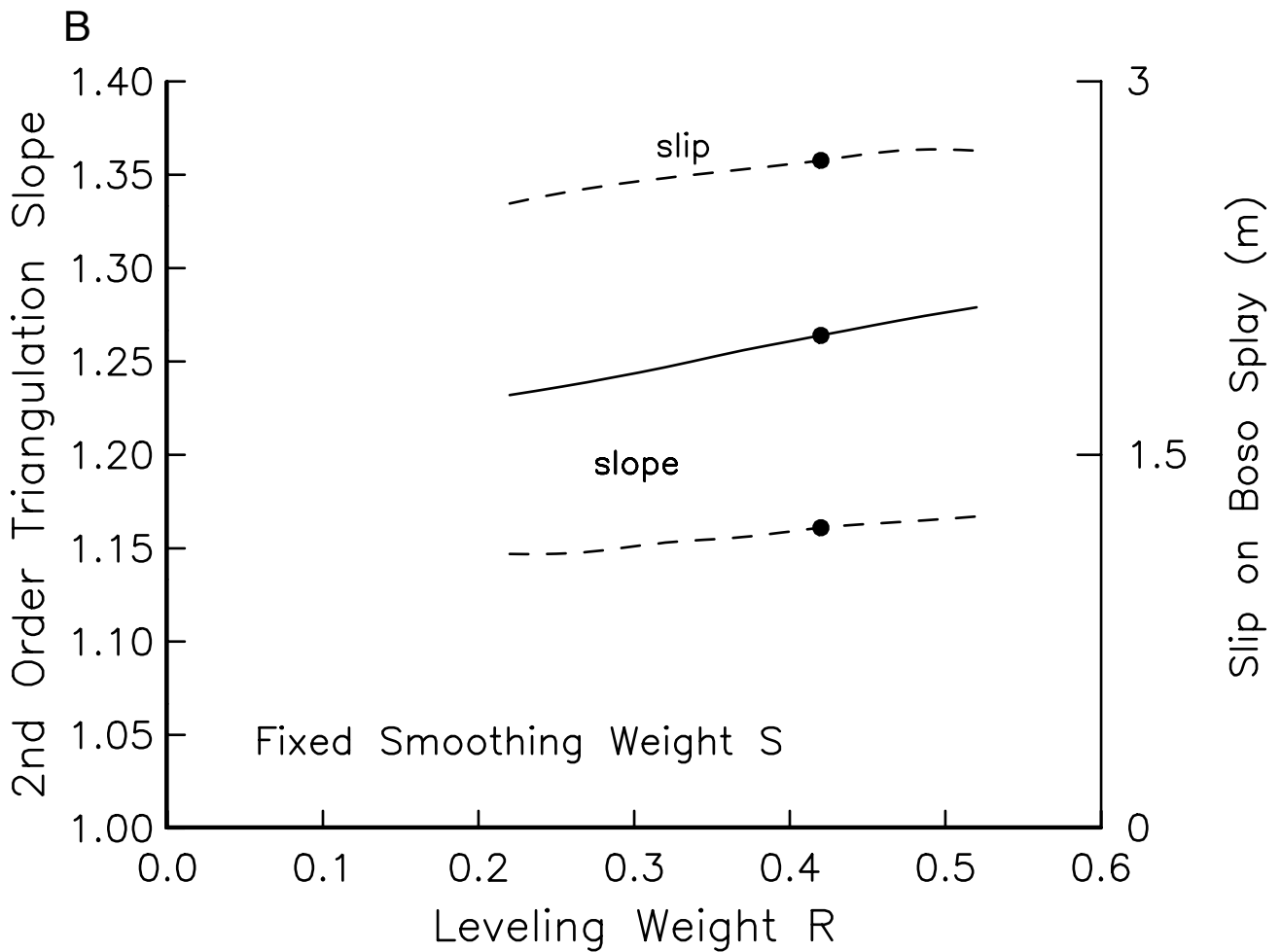
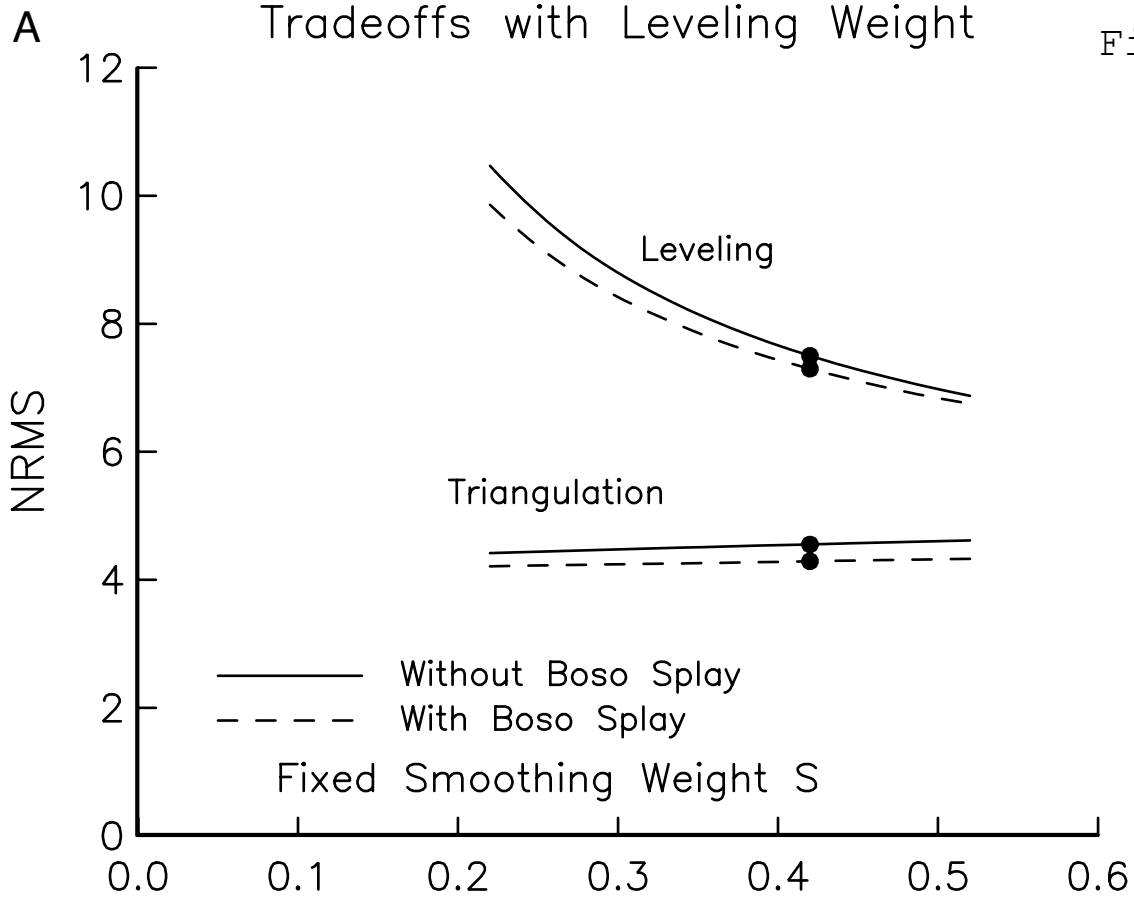


Figure 9



# Tradeoffs with Leveling Weight

Figure 10



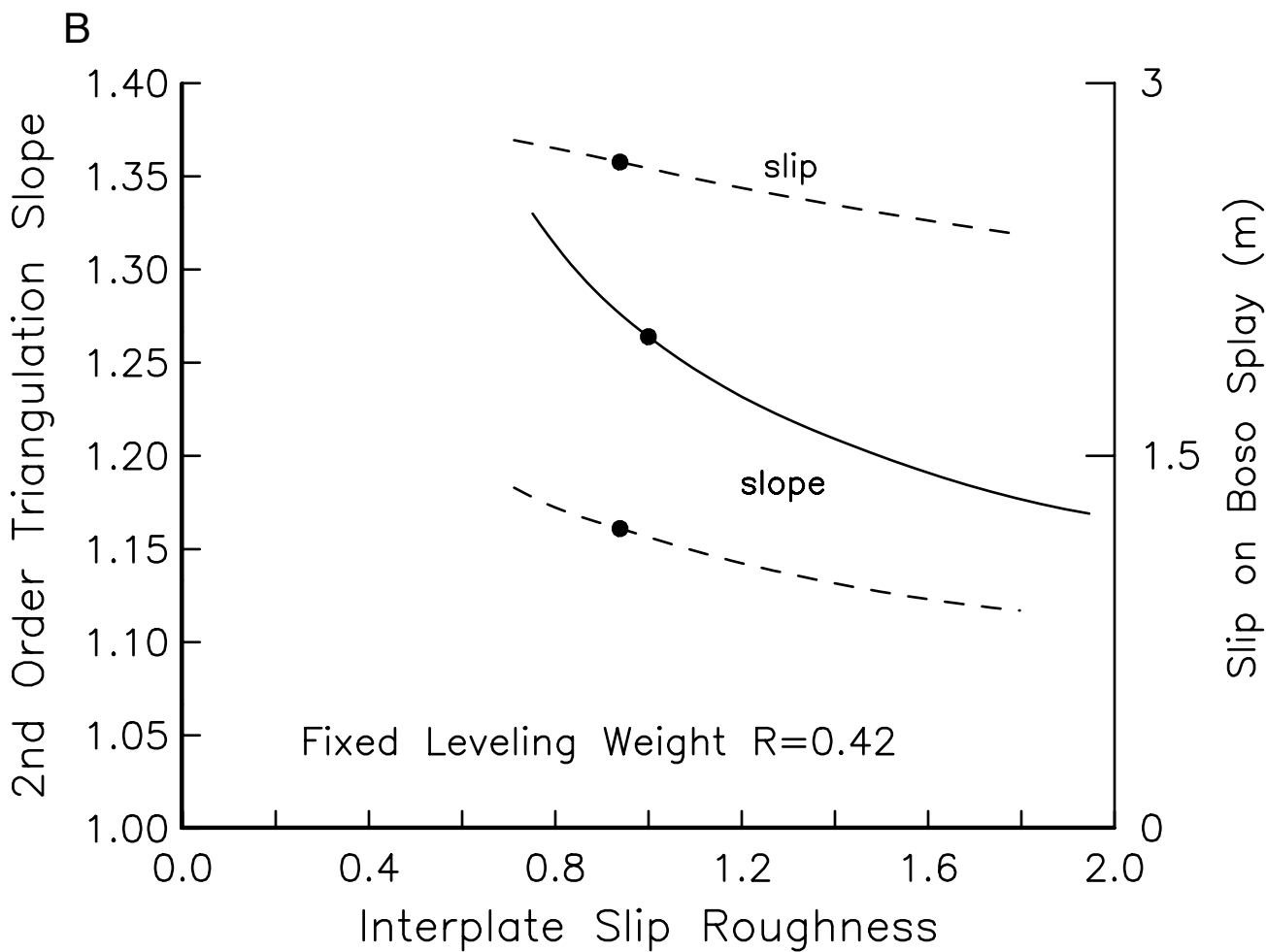
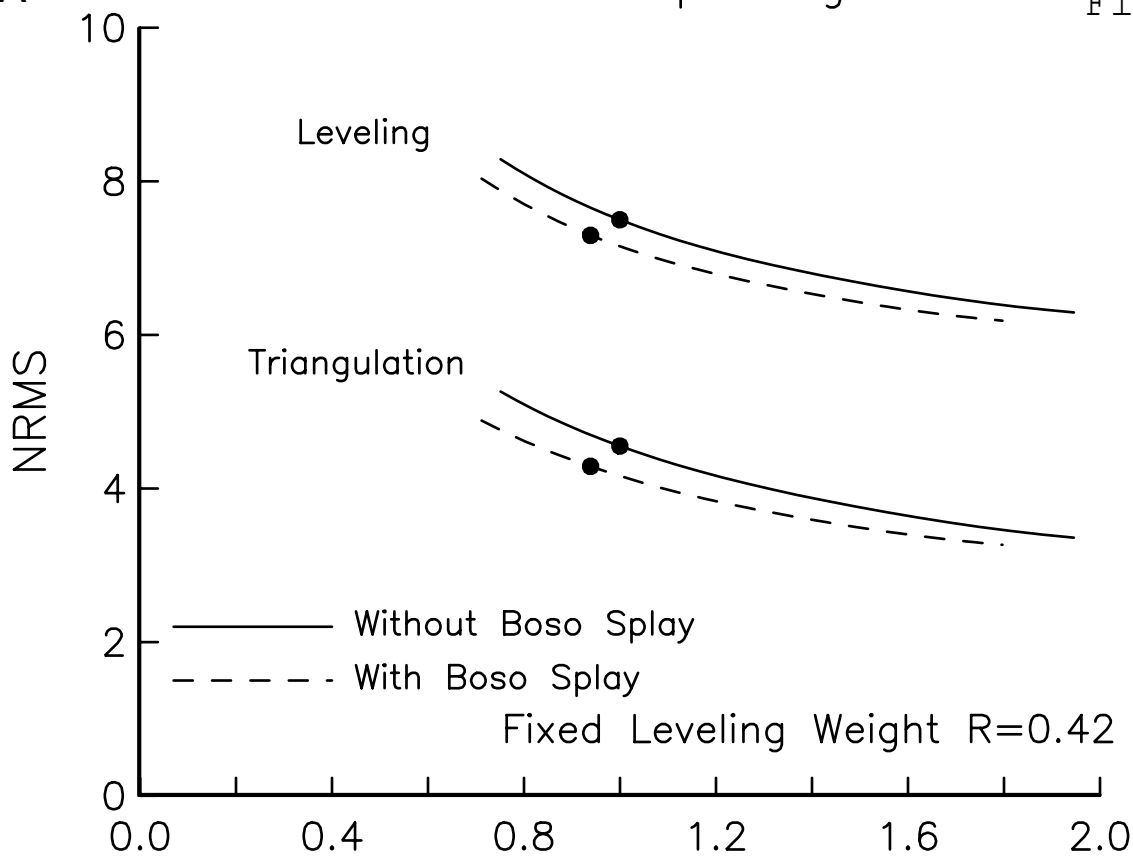


Figure 12

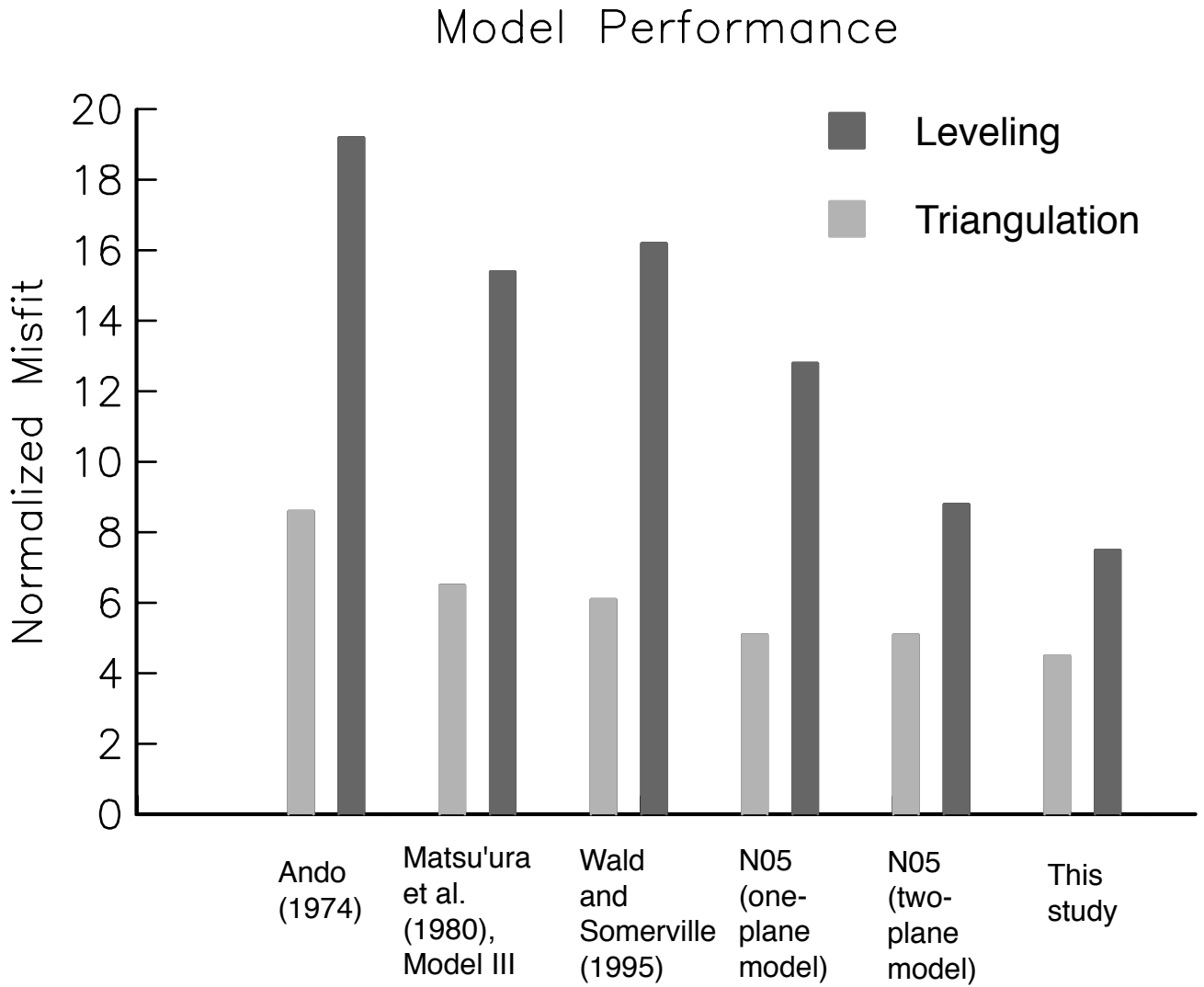
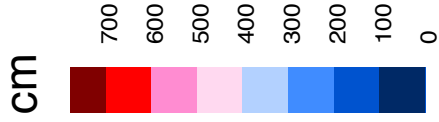
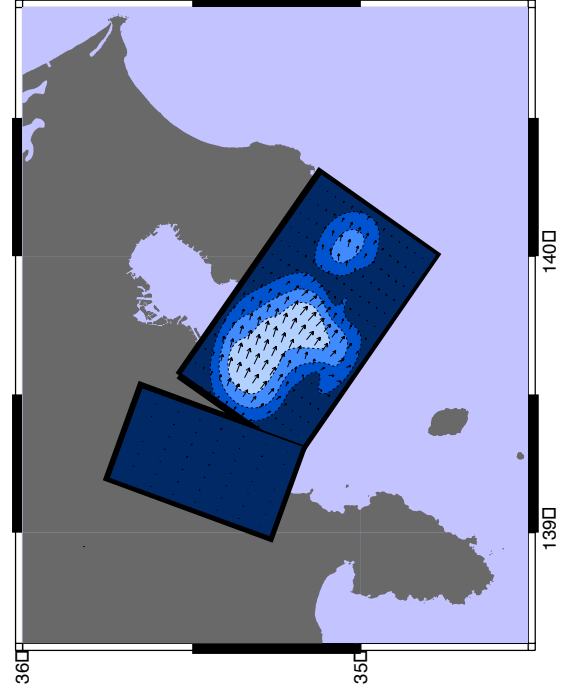
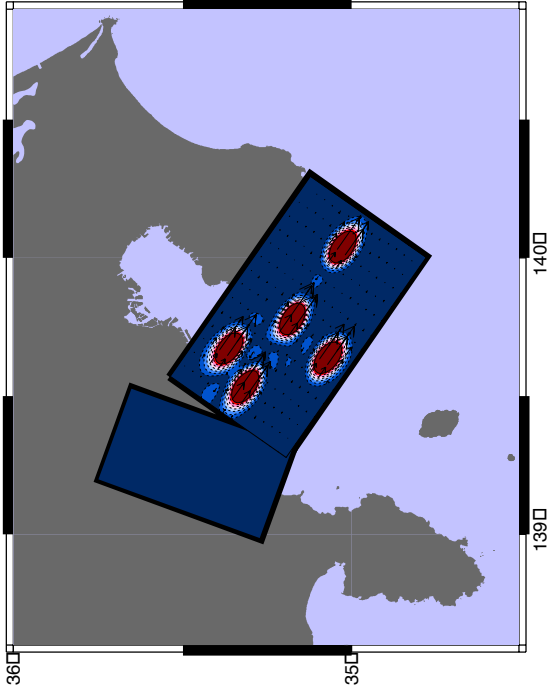
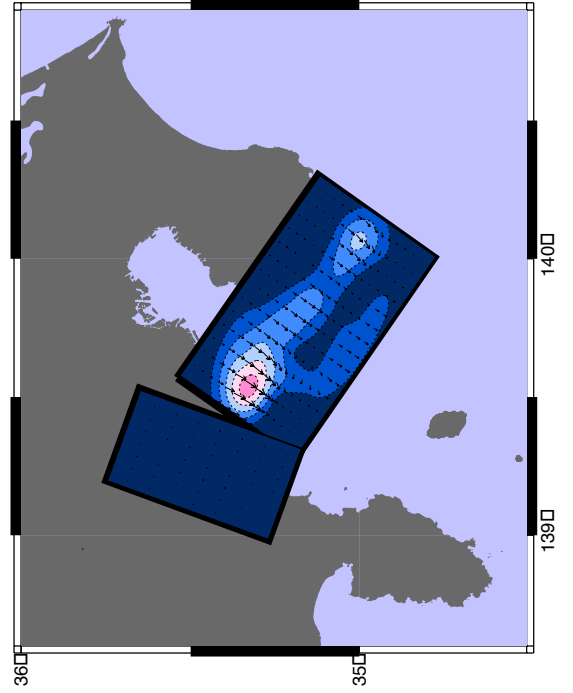
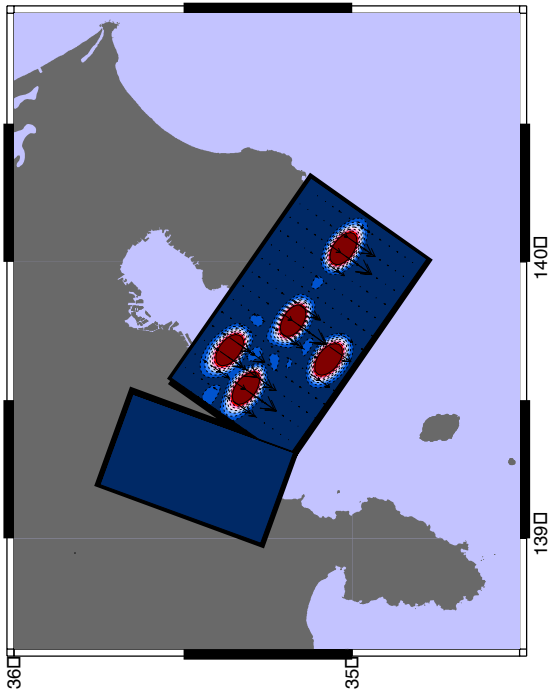


Figure 13

Strike-slip



Dip-slip



Input

Inverted



Figure 14

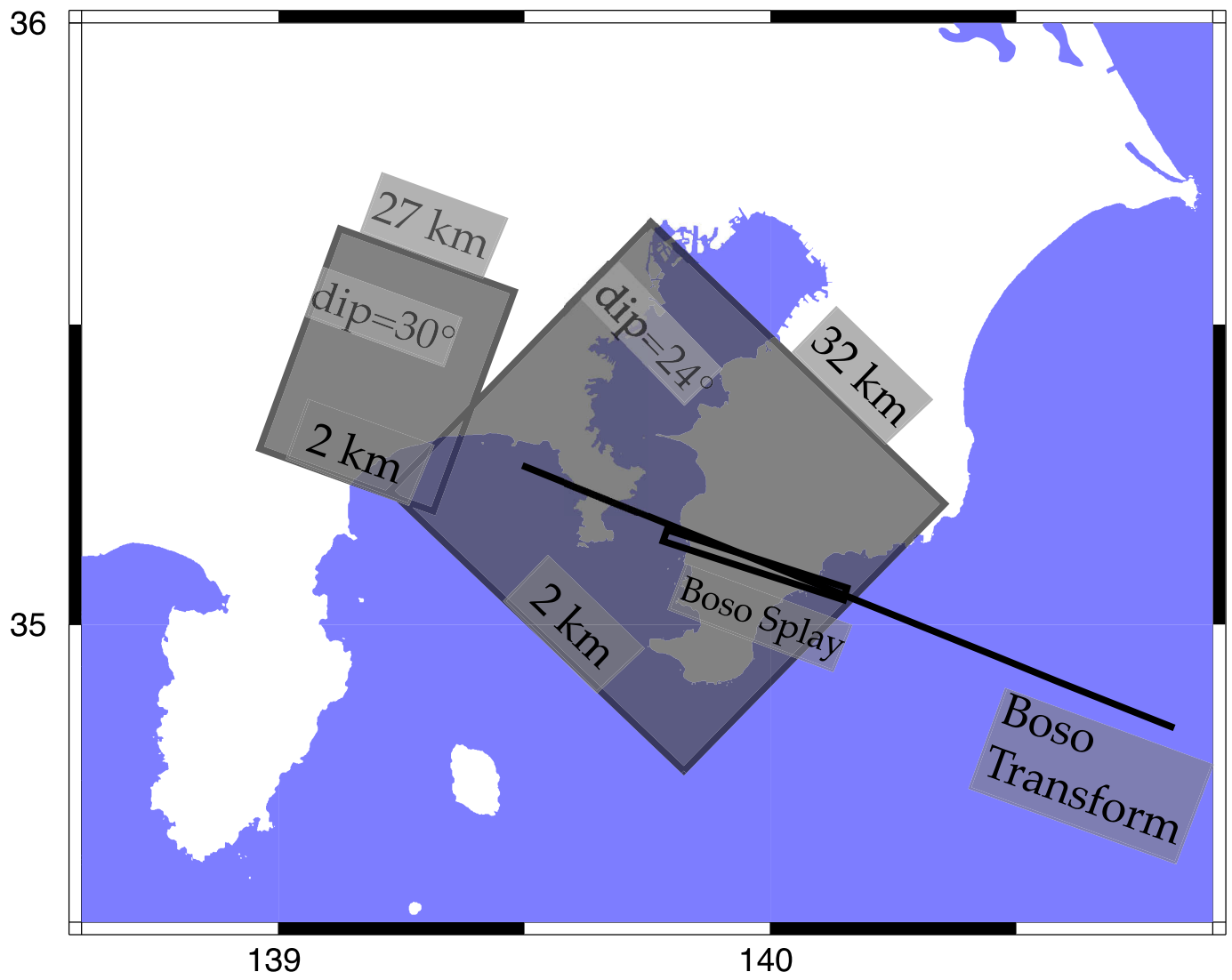


Figure 15

### Alternative planes + Boso transform

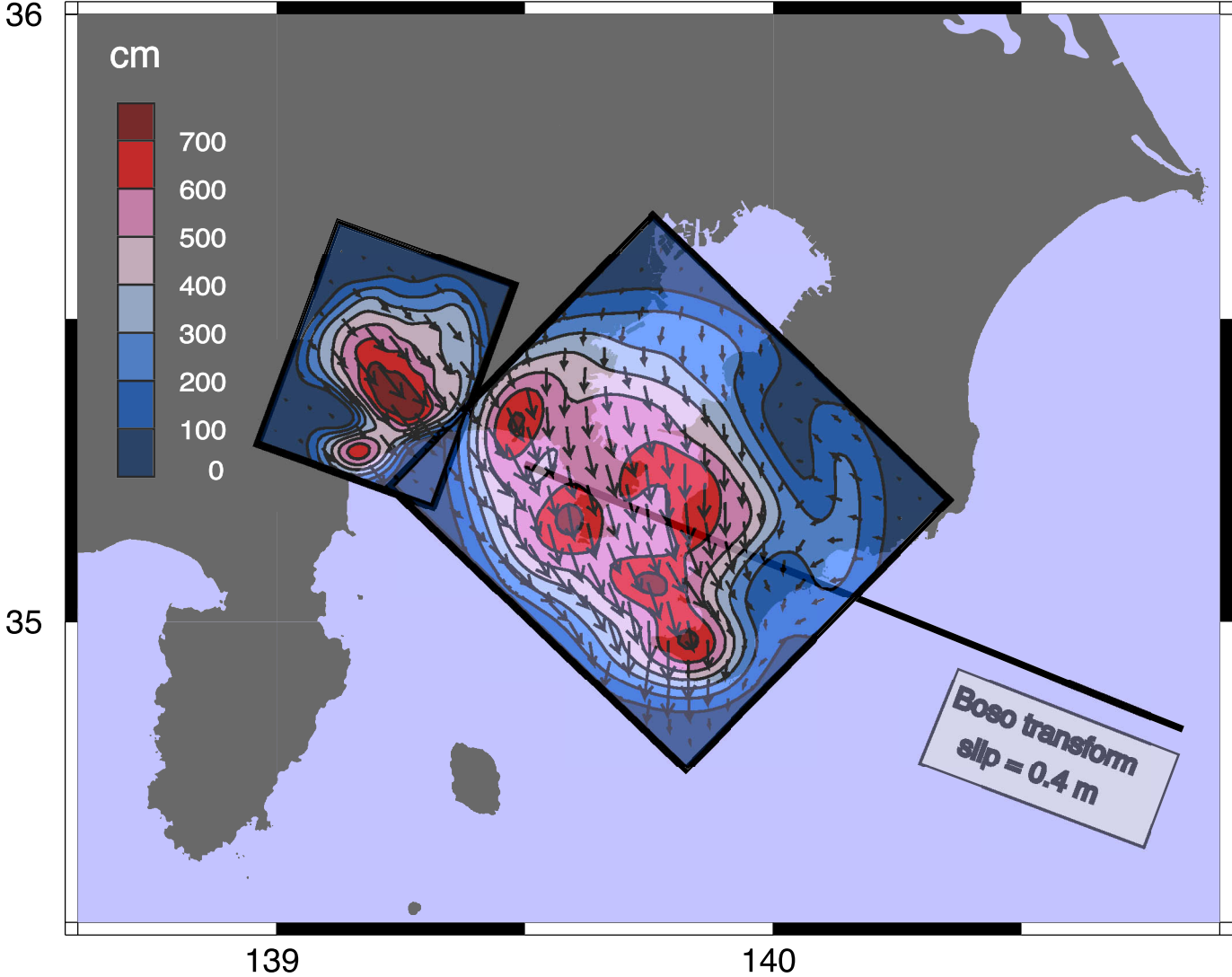


Figure 16

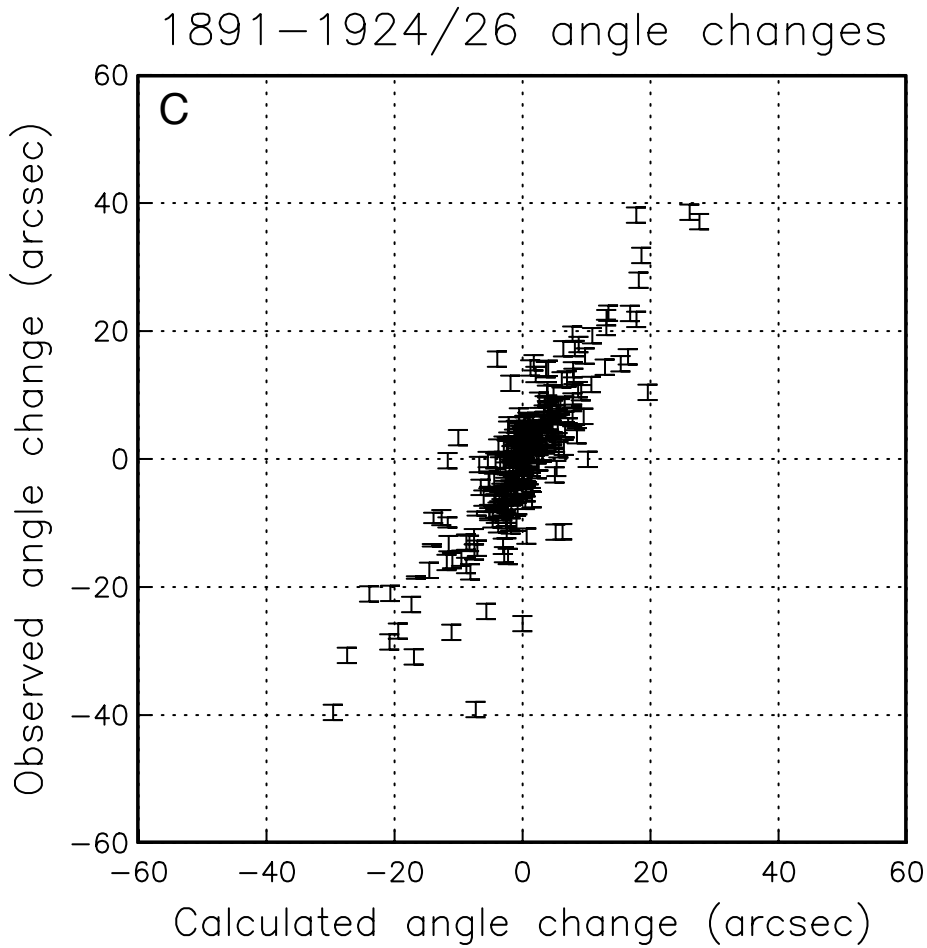
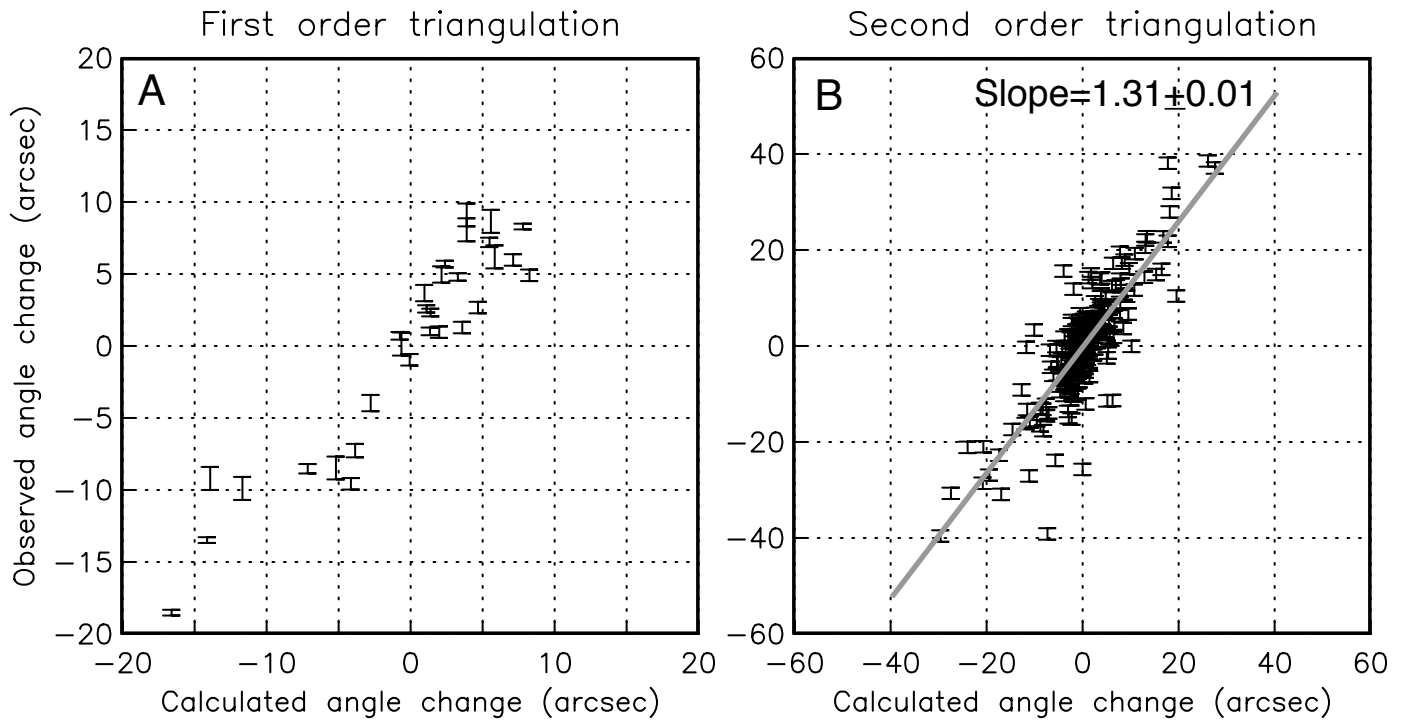
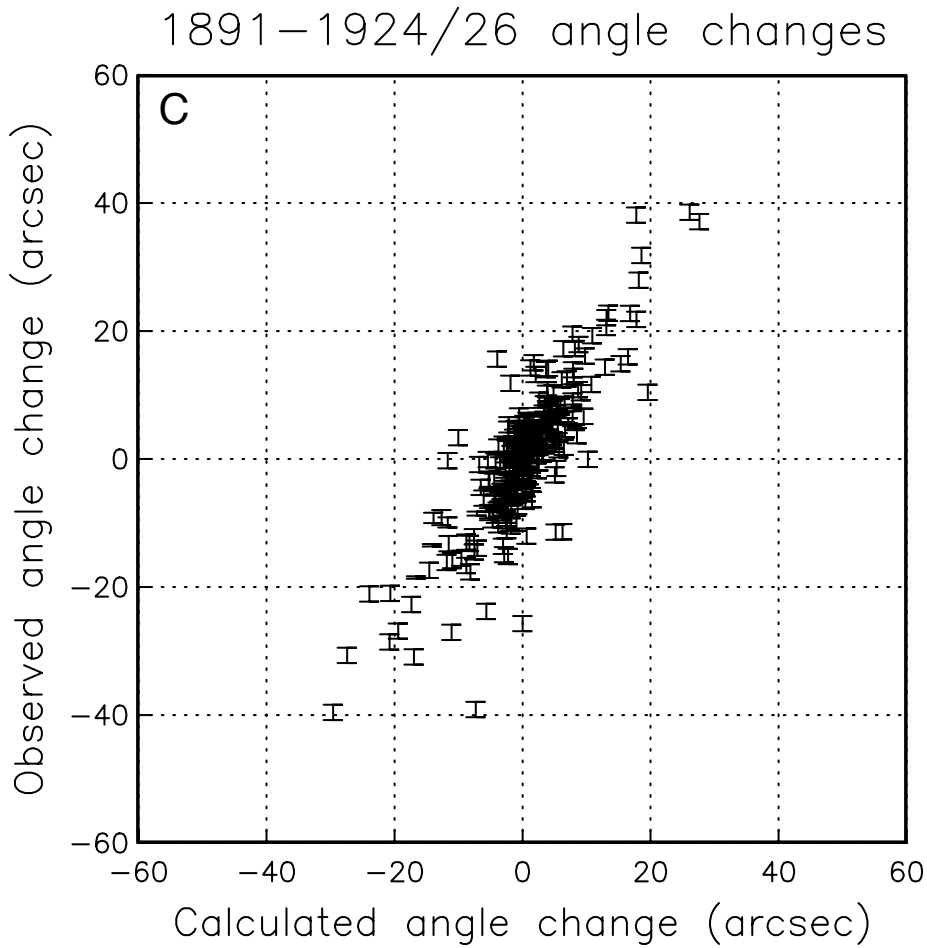
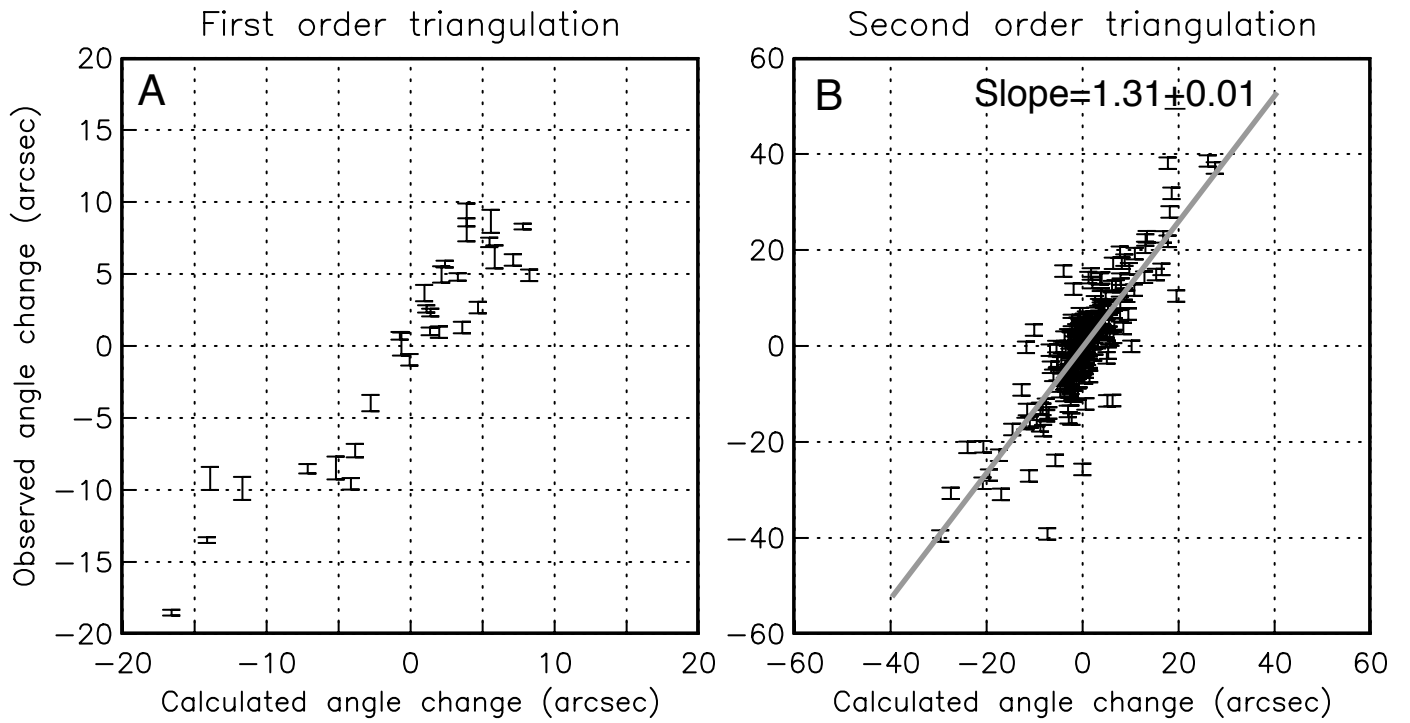
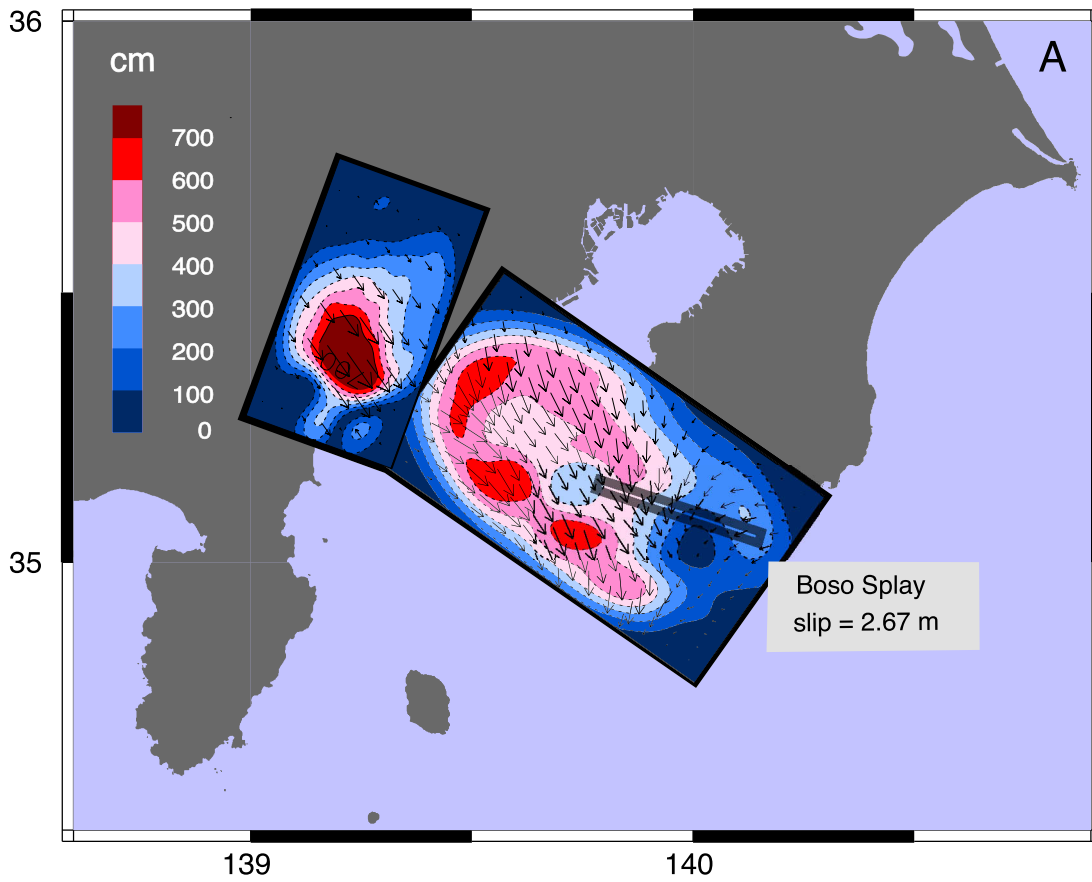


Figure 16



Extended N05 planes + Boso Splay

Figure 17



Alternative planes + Boso Splay

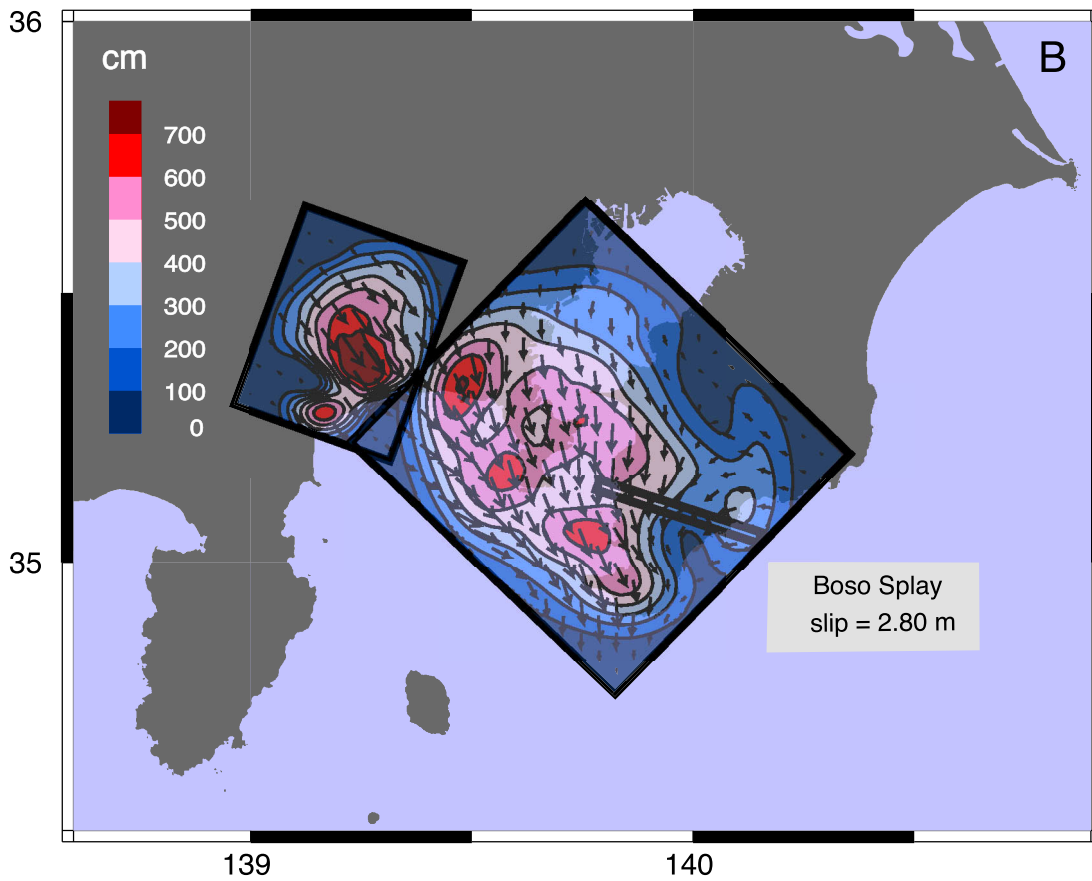
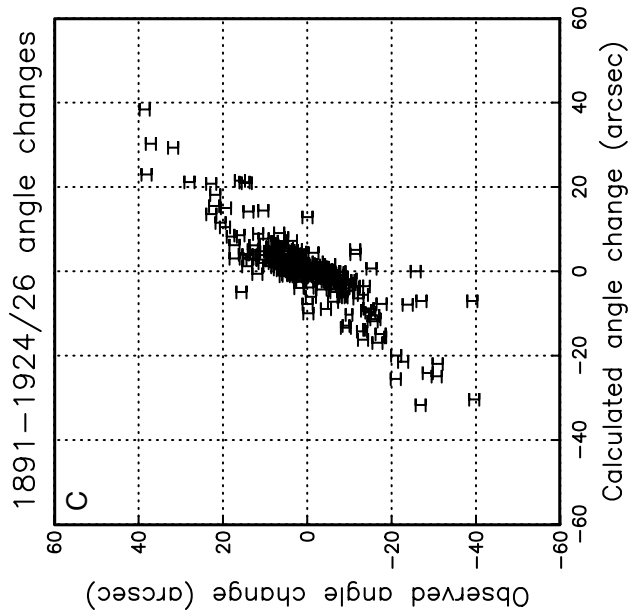
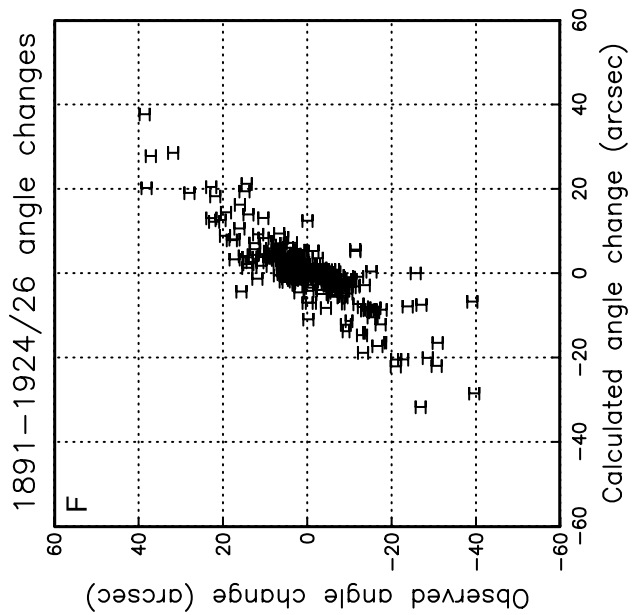
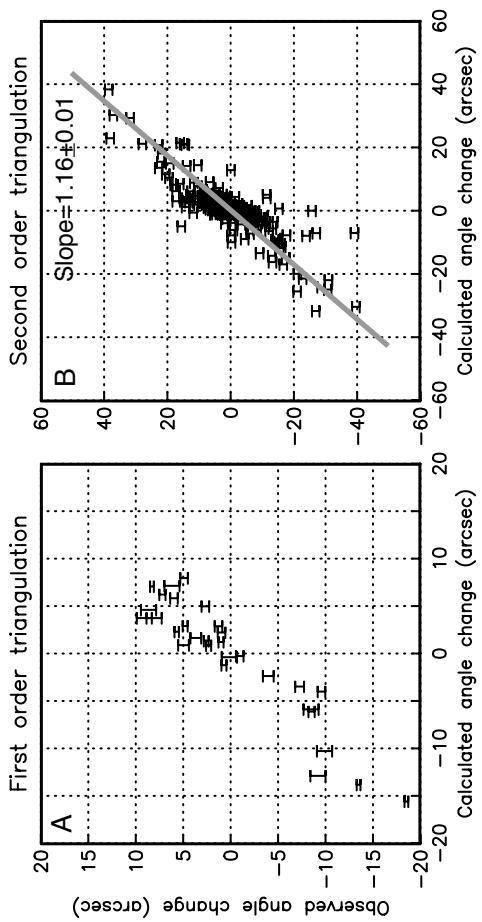
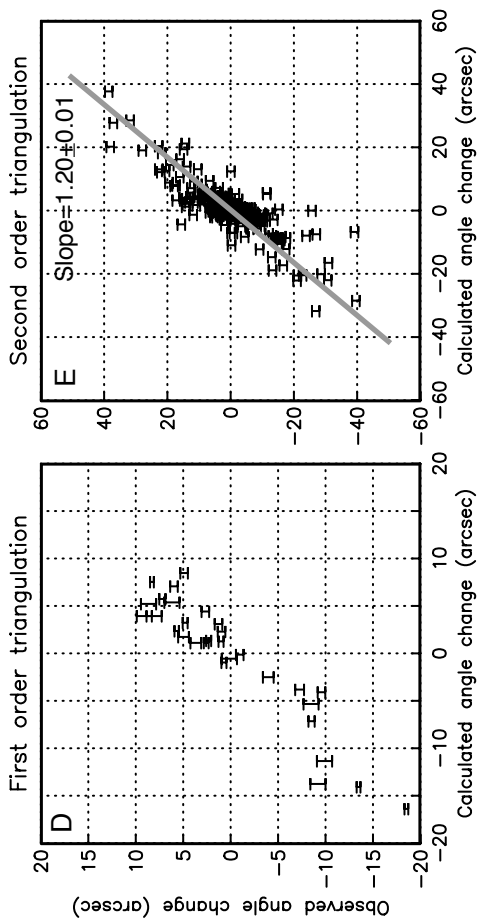
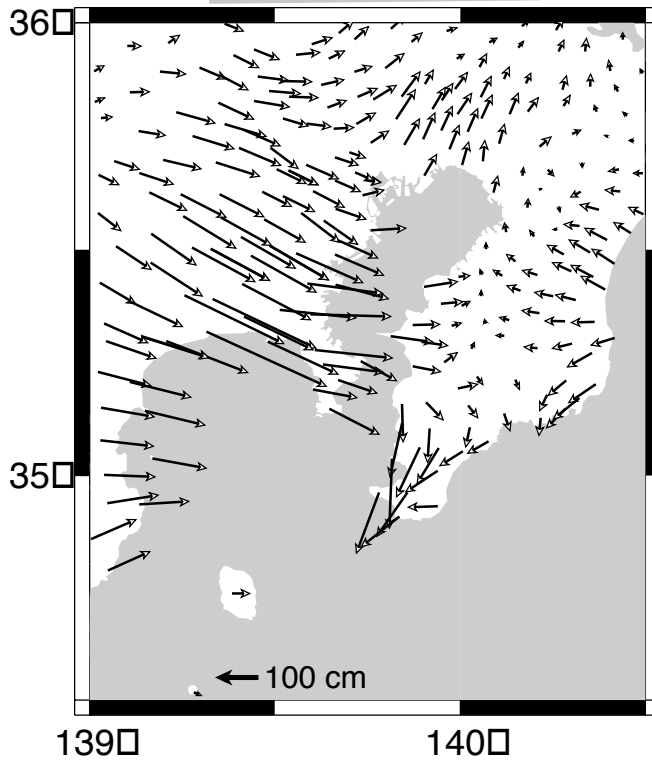


Figure 18



### A Displacement



### B Deviatoric shear

### Deviatoric shear

